Journal of Cosmology and Astroparticle Physics
An IOP and SISSA journal

Received: *September 1, 2025*
Accepted: *November 27, 2025*
Published: *January 22, 2026*

Indirect searches for realistic sub-GeV Dark Matter models

Marco Cirelli,[a] **Arpan Kar**[a] **and Halim Shaikh**[b]

[a] *Laboratoire de Physique Théorique et Hautes Énergies (LPTHE),*[1]
CNRS & Sorbonne Université,
4 Place Jussieu, Paris, France
[b] *Fulbari, Karimpur, Nadia, West Bengal, 741158, India*

E-mail: marco.cirelli@gmail.com, arpankarphys@gmail.com, halimshaikh109@gmail.com

Abstract: Indirect searches for Dark Matter (DM) particles with mass in the MeV–GeV scale have received significant attention lately. Pair-annihilations of such DM particles in the Galaxy can give rise to (at the same time) MeV to GeV γ-rays via prompt emission, sub-GeV $e^{\pm}$ in cosmic-rays, as well as a broad photon spectrum ranging from X-rays to soft γ-rays, produced by the DM induced $e^{\pm}$ via inverse Compton scattering, bremsstrahlung and in-flight annihilation processes (collectively called 'secondary emissions'). We focus on two representative realistic sub-GeV DM models, namely, the vector-portal kinetic-mixing model and the higgs-portal model, and perform a detailed study of the indirect detection constraints from existing X-rays, γ-rays and cosmic-ray observations, based on all of the above-mentioned signals. We also estimate the future prospects from the upcoming MeV photon telescope Cosi, including all possible types of prompt and secondary emission signals. We compare our results with the constraints and (or) projections from cosmological and terrestrial observations. We find that, for both the sub-GeV DM models, the current observations constrain the annihilation cross-section at the level of $\langle\sigma v\rangle \lesssim 10^{-27}\,\mathrm{cm}^3/\mathrm{s}$, or lower for some specific mass ranges or under optimistic assumptions. Moreover, new unconstrained DM parameter space can be probed at the upcoming instruments like Cosi, thanks to the inclusion of secondary photons which in many cases provide the dominant signal.

Keywords: dark matter theory, gamma ray experiments, X-ray telescopes, cosmic ray experiments

ArXiv ePrint: 2508.03819

[1] LPTHE — https://www.lpthe.jussieu.fr, https://ror.org/02mph9k76.

https://doi.org/10.1088/1475-7516/2026/01/038

JCAP01(2026)038

Contents

1 Introduction

The idea that Dark Matter (DM) could be composed of a light particle, where light refers to a mass $m_{\rm DM}$ in the range of approximately 1 MeV to a few GeVs, has recently gathered significant attention. This interest stems partly from the absence of compelling evidence for the long-predicted weak-scale DM in current experiments, and partly from the rise of well-motivated theoretical models that predict such sub-GeV DM candidates (see for instance [1–10] for a selection of recent works).

The indirect detection of sub-GeV DM (i.e. the searches for the products of annihilations — or decays — of such particles in astrophysical environments) is a particularly promising, and somewhat still under-exploited, direction.

JCAP01(2026)038

From the observational point of view, the signals that can be looked for are essentially of three kinds:[1] *(1)* MeV to GeV gamma rays emitted as prompt radiation from the DM annihilations, *(2)* sub-GeV electrons and positrons (collectively denoted in the following as $e^{\pm}$), emitted from the same annihilation processes, *(3)* soft gamma rays or keV X-rays emitted as secondary radiation from these $e^{\pm}$ in the astrophysical environment.

From the phenomenological point of view, the analysis of these signals can be carried out in essentially two ways: *(a)* a model-independent one, i.e. considering the annihilation of DM particles into representative channels such as $\gamma\gamma$, e^+e^-, $\mu^+\mu^-$ or $\pi^+\pi^-$, without committing to any specific particle physics realization; *(b)* a model-specific one, i.e. assuming a fixed model of DM and a determined annihilation process into realistic final states, consisting of light hadronic resonances such as $\pi, \eta, K, \rho, \omega, \phi \ldots$. The former approach has the advantage of being general and flexible. The latter, however, is instead particularly well motivated for sub-GeV DM: at these low energies, which are comparable to the QCD confining scale, the light mesons cited above *are* the relevant degrees of freedom in the final state of the annihilation (this is in contrast to heavier DM models — above several GeVs — in which the annihilation into quarks and gauge bosons describes well the process).

A number of works in the recent literature have tackled the indirect detection of sub-GeV DM along these observational and phenomenological axes. For the sake of setting the stage of the context of our study, we list here a selection of these works, making explicit references to the signals *(1)*, *(2)* or *(3)* and to the approaches *(a)* or *(b)* above.

Ref. [11] studied the bounds from prompt photons (signal *(1)* above) measured by several MeV experiments, for a few generic channels (approach *(a)*). Later on, ref. [12–15] considered the future prospects for the same signals, as did ref. [16], adding also secondary radiation *(3)*. Refs. [17, 18] derived bounds from Voyager-1 data on $e^{\pm}$ (signal *(2)* above), from generic annihilation channels *(a)*. Ref. [19] considered the prompt monochromatic photons *(1)* from the annihilation in the $\gamma\gamma$ channel *(a)*, using Integral data. Refs. [20–22] computed the constraints from prompt *(1)* and secondary *(3)* radiation, in a model-independent *(a)* approach, using X-ray data from Integral, NuStar, Xmm-Newton, eRosita and other experiments. Ref. [23] also included $e^{\pm}$ Voyager-1 data *(2)*. Ref. [24, 25] worked out the current and projected limits from prompt photons *(1)*, as well as from the Cosmic Microwave Background (CMB), for higgs-portal and dark-photon-portal models, within approach *(b)* above. Similarly, ref. [26] considered prompt photons *(1)* in an $(L_\mu - L_\tau)$ vector-mediator model, and ref. [27] in leptophilic DM models. Ref. [28] considered prompt photons *(1)* and $e^{\pm}$ *(2)* in specific effective models, and ref. [29] did the same for decaying DM. Ref. [30] adds secondary radiation *(3)*, always for decaying DM. Other recent studies on the broad phenomenology of sub-GeV detection include [31–35].

What this quick survey shows is that a study following the theoretically motivated approach *(b)* for annihilating DM, and considering all the *(1)*, *(2)* and *(3)* signal classes is currently missing.

[1] We focus the discussion, from now on, on annihilating sub-GeV DM, since this is the natural choice for the models we consider later. But our general analysis can be easily extended to the case of decaying sub-GeV DM as well.

JCAP01(2026)038

The main focus of this work is therefore the following: focusing on representative realistic sub-GeV DM models, we perform a detailed study of the indirect detection constraints based on the existing photon and cosmic-ray observations, and we evaluate the future prospects from upcoming MeV photon telescopes like COSI, by including all possible types of prompt and secondary emission signals related to DM annihilations in the Galaxy.

The rest of this paper is organized as follows. In section 2 we introduce the two classes of sub-GeV DM models that we consider in the following. In section 3 we discuss the primary and secondary photon signals produced in the Galaxy from the annihilation of sub-GeV DM particles under such models. In section 4 we discuss the corresponding cosmic-ray $e^{\pm}$ signal from DM annihilation. In section 5 we discuss different observed data and describe the analysis methods. Section 5.3 contains a discussion on the upcoming MeV telescope COSI. In section 6 we presents our results and the corresponding discussions as well as the comparison with other constraints and projections. Finally, in section 7 we summarize our results and draw our conclusions. Appendix A offers some complementary technical details on secondary emissions, while appendix B evaluates the impact of choosing different DM profiles.

2 Models of sub-GeV Dark Matter

In this section we introduce the two well-motivated sub-GeV particle DM models that we will consider in the following: a model featuring a vector mediator kinetically mixing with the Standard Model (SM) photon (section 2.1), and a scalar mediator mixing with the SM higgs (section 2.2). They are representative of generic classes: the vector-portal class [26, 36–38] and the scalar-portal class [27, 37, 39, 40], characterized by the fact that the DM particle interacts with the SM particles through a vector or a scalar mediator, respectively. And they correspond to two kinds of 'portal' interactions routinely considered in the literature, see e.g. [41–43]. In both cases we consider the DM to be a Dirac fermionic particle for definiteness, and we take both the DM and the mediator to be uncharged under the SM gauge group. We also assume symmetry between DM particles and antiparticles.

These sub-GeV DM models are implemented in the publicly-available code `HAZMA` [24, 44] and in its updated version `HAZMA2` [45]. The codes provides accurate spectra of photons, electrons and positrons, and neutrinos produced in the pair-annihilation of DM particles. The spectrum of photons (produced via prompt emission) leads to the primary photon signals for indirect detection. The $e^{\pm}$ spectra, on the other hand, give rise to an analogous primary charged cosmic-ray signal but also to various secondary photon signals (which in many cases become stronger than the primary). These different signals will be discussed in sections 3 and 4.

As mentioned in the introduction, in realistic sub-GeV DM models, where the annihilation typically occurs into more than one final state, the relevant final-state degrees of freedom are combinations of light hadronic resonances [44, 45].[2] `HAZMA`, using chiral perturbation theory, computes the corresponding annihilation cross-sections (or the branching fractions of the total cross-section) as well as the final-state spectra up to a DM mass of 250 MeV. The updated

[2]Note that the annihilation spectra obtained from the widely-used tool `PYTHIA` [46, 47] are reliable at center-of-mass energy above a few GeV, but not at lower energies, where strongly-interacting particles form hadronic bound states and can no longer be effectively described by parton showers, fragmentation and decay.

JCAP01(2026)038

version HAZMA2 [45] extends the range and provides the same outputs up to a center-of-mass energy of the DM annihilation of about 3 GeV (i.e. DM mass of 1.5 GeV). This is achieved in HAZMA2 by bridging the regimes of validity of HAZMA1 with that of another state of the art tool, HERWIG4DM [48, 49], which is based on vector meson dominance and measured form-factors, and is accurate well up to a few GeVs. Altogether, these tools allow to compute the indirect detection spectra in the whole mass range of out interest, between 1 MeV and 1 GeV.

We now move to describe more precisely the two sub-GeV DM model classes analyzed in this work. See also [24, 25, 44, 45] for the further detailed discussions.

2.1 Vector portal: dark photon or kinetic-mixing model

We consider a simplified model featuring a DM particle (a Dirac fermion for definiteness, as mentioned earlier) charged under a new $\mathrm{U}(1)_D$ dark gauge group, whose vector boson V mixes with the SM photon. The model is fully defined by the following parameters: the mass $m_{\rm DM}$ of the DM particle, the mass m_V of the vector mediator V, the coupling of the vector mediator to DM ($g_{V\rm DM}$) and the kinetic mixing parameter ϵ between the vector mediator and the SM photon. The couplings of V to the SM fermions are inherited from those of the photon and, explicitly, are given by $g_{Vf} = \epsilon e Q_f$, where Q_f is the electric charge of the fermion f and e is the electron's charge. We assume the mediator's mass to be $m_V = 3\, m_{\rm DM}$, for which most of the terrestrial constraints and future projections on this model (for sub-GeV DM masses) are usually available; see, for example, [41, 42, 50–52]. This choice of the mediator's mass corresponds to the scenario dominated by 'Direct Annihilation', where the annihilation of DM particles proceeds via $\mathrm{DM\,DM} \to V^* \to f\bar{f}$ to SM fermions through the virtual mediator. The total pair-annihilation cross-section of DM in this case is [41, 42]:

$$\langle \sigma v \rangle \propto \epsilon^2\, \alpha_D\, \frac{m_{\rm DM}^2}{m_V^4} = \frac{y}{m_{\rm DM}^2}\,, \qquad \text{with} \quad y = \epsilon^2\, \alpha_D \left(\frac{m_{\rm DM}}{m_V}\right)^4\,, \tag{2.1}$$

where $\alpha_D = g_{V\rm DM}^2/4\pi$. Note that here the DM annihilation proceeds through s-wave.

As discussed above, we obtain the DM-induced annihilation spectra of $e^\pm$ and photons using HAZMA. A few examples of the $e^\pm$ spectrum $\frac{dN_e}{dE_e}\Big|_{\rm tot}$ for different DM masses ($m_{\rm DM} =$ 30, 300 and 700 MeV) are shown in the left panel of figure 1. Here $\frac{dN_e}{dE_e}\Big|_{\rm tot} = \sum_F B_F\, \frac{dN_e^F}{dE_e}$ is the total spectrum as a sum of the contribution from each (kinematically possible) annihilation channel F with the corresponding branching fraction B_F. The spectra consist of two main components. A sharp peak component, coming from the mediator (V^*) decaying into $e^+\, e^-$, dominates for lower $m_{\rm DM}$'s and at higher energies for larger $m_{\rm DM}$'s. There is an additional smooth component (relevant for comparatively larger $m_{\rm DM}$'s), coming from mediator decays into muons and combinations of light mesons, which dominates the low energy part of the spectrum. See ref. [45] for details. Note that in our parameter setup ($m_V = 3\, m_{\rm DM}$) the spectra $\frac{dN}{dE}\Big|_{\rm tot}$ depend only on $m_{\rm DM}$ (or m_V), but not on the choice of $g_{V\rm DM}$ or ϵ,[3] since the

[3] In general, $\frac{dN}{dE}\Big|_{\rm tot} = \sum_F B_F \frac{dN^F}{dE}(m_{\rm DM}) = \sum_F \frac{\langle\sigma v\rangle_F}{\langle\sigma v\rangle_{\rm tot}} \frac{dN^F}{dE}(m_{\rm DM})$. Here $\frac{dN^F}{dE}$ is the γ or e^+ spectrum produced in the SM channel F and depends only on the outgoing energy in the channel F (i.e., on the DM mass) but not on the DM couplings. In the case with $m_V = 3\, m_{\rm DM}$, the only kinematically allowed annihilation channels are $\mathrm{DM\,DM} \to V^* \to f\bar{f}$, for which $\langle\sigma v\rangle_F \propto (\epsilon\, g_{V\rm DM})^2$ (see eq. (2.1)), and hence $\langle\sigma v\rangle_{\rm tot} = \sum_F \langle\sigma v\rangle_F \propto (\epsilon\, g_{V\rm DM})^2$. As a result, the spectra $\frac{dN}{dE}\Big|_{\rm tot}$ are independent on $g_{V\rm DM}$ or ϵ.

JCAP01(2026)038

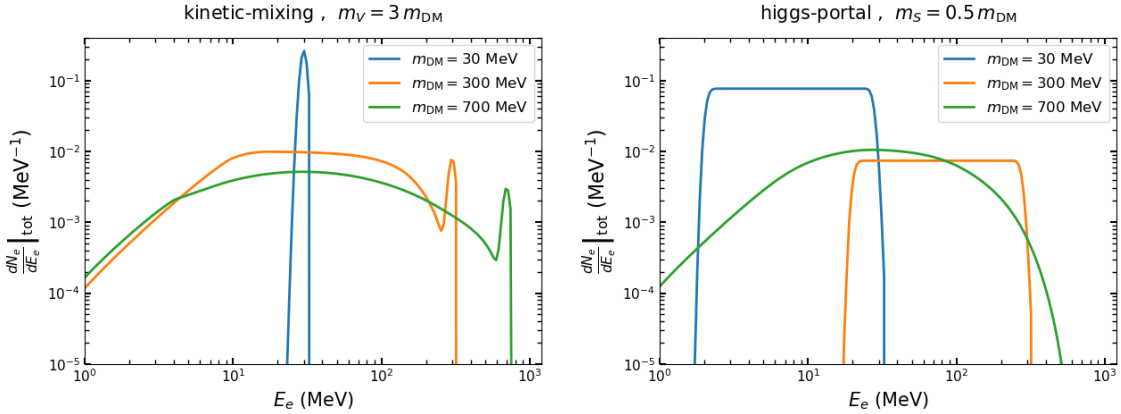

Figure 1. Total electron or positron *spectra* $\left.\frac{dN_e}{dE_e}\right|_{\rm tot}$ as a function of E_e for different values of $m_{\rm DM}$, considering the kinetic-mixing model with $m_V = 3\,m_{\rm DM}$ (left panel) and higgs-portal model with $m_S = 0.5\,m_{\rm DM}$ (right panel). In each case, we add a 5% resolution in the $e^{\pm}$ energy.

latter parameters enter only in determining the strength of V^* production and decay. In the opposite regime ($m_V < m_{\rm DM}$), the competing annihilation channel DM DM $\to VV \to f\bar{f}f'\bar{f}'$ ('Secluded Annihilation') opens up, producing different spectra, and the interplay among the two processes (hence the total spectra) depends on all parameters.

2.2 Scalar portal: higgs-portal model

We consider a simplified model featuring a scalar mediator S that mixes with the SM higgs boson. Like in the case of the kinetic-mixing model, here, too, it is assumed that the scalar mediator interacts with the SM particles only via its mixing with the SM higgs. The model is fully defined by the following parameters: the mass $m_{\rm DM}$ of the DM particle, the mass m_S of the scalar mediator S, the coupling of the mediator to DM ($g_{S\rm DM}$) and the mixing angle ϑ between the scalar mediator and SM higgs. The couplings of the mediator to the SM fermions, gluons and photon are inherited from those of the SM higgs. Namely, they are the same as those of the SM higgs except that they are suppressed by a factor $\sin\vartheta$. We assume the scalar mediator mass to be $m_S = m_{\rm DM}/2$, i.e. lower than the DM mass. In the other case, where the mediator is heavier than the DM, different terrestrial search constraints are expected to dominate over those coming from indirect detection searches (see, e.g., [24, 25]). In the case that we consider, the annihilation of DM into SM particles is dominated by the process DM DM $\to SS$ followed by the decay of S into SM particles. The corresponding total pair-annihilation cross-section is [39]:

$$\langle\sigma v\rangle = \frac{3\,g_{S\rm DM}^4\,v_{\rm rel}^2}{128\,\pi\,m_{\rm DM}^2}\,, \tag{2.2}$$

with $v_{\rm rel}$ being the relative velocity of the two annihilating DM particles. Note that here $\sin\vartheta$ plays no role (so the thermal freeze-out is compatible with a wide range of values of ϑ) and the DM annihilation proceeds through p-wave. For this model we will present (in section 6) all constraints on $\langle\sigma v\rangle$ that corresponds to our galaxy (with $v_{rel} \simeq 220\,$km/s).

JCAP01(2026)038

A few examples of the total $e^{\pm}$ spectrum $\left(\frac{dN_e}{dE_e}\Big|_{\rm tot}\right)$ in this model are shown in the right panel of figure 1 for different DM masses ($m_{\rm DM} = 30, 300$ and $700\,{\rm MeV}$). The spectra consist of a box component coming from the *on-shell* mediator S decaying into $e^+\,e^-$ (which dominates at lower DM masses for $m_{\rm DM}$ above the electron threshold, $2\,{\rm MeV}$), and a smooth component coming from S decaying into muons and pions (which is dominating at higher DM masses). See [24, 25, 44] for details. Note that in our parameter regime ($m_S = m_{\rm DM}/2$) the spectra $\frac{dN}{dE}\Big|_{\rm tot}$ for $e^{\pm}$ or photon depends only on $m_{\rm DM}$ (or m_S), but not on the choice of $g_{S\rm DM}$ or $\sin\vartheta$ (at least for not-too-extreme values of these parameters, otherwise the competing annihilation channel DM DM $\to S \to f\bar{f}$ becomes relevant and, since it depends $g_{S\rm DM}$ and $\sin\vartheta$, the total spectra are modified).[4]

In the next two sections we discuss various possible indirect detection signals that can arise due to the annihilation of sub-GeV DM particles under a realistic model. These discussions on signals will be focused on the kinetic-mixing DM model discussed in the previous sub-section, for definiteness, but they are easily generalized to the other DM models.

3 Photon signals from sub-GeV DM annihilation in the inner Galaxy

In this section we discuss the photon signals from the annihilation of sub-GeV DM in the inner Galaxy. We assume that the density distribution of DM in the galactic halo is described by the NFW profile [53]:

$$\rho_{\rm DM}(r) = \frac{\rho_0}{\left(\frac{r}{r_s}\right)\left(1+\frac{r}{r_s}\right)^2}\,, \tag{3.1}$$

with r as the radial distance from the galactic center (GC). For the parameters ρ_0 and r_s we consider the values $\rho_0 = 0.839\,{\rm GeV\,cm^{-3}}$ and $r_s = 11\,{\rm kpc}$, which correspond to the fitted NFW profile parameters (the central values) obtained in [54] for the baryonic model B2. However, for comparison we will also consider other choices for the DM profile, see appendix B.

The photon energy range considered in this work is $10\,{\rm keV} \lesssim E_\gamma \lesssim 1\,{\rm GeV}$ which includes the existing observations by Integral, Comptel, Egret and Fermi-Lat (partially) as well as the future observation by the MeV telescope Cosi. As for the region of observation (ROI), we consider areas of different sizes (centered on the GC) corresponding to different experimental observations, i.e., $|b| < 15°, |l| < 30°$ for Integral, $|b| < 20°, |l| < 60°$ for Comptel, $|b| < 10°, |l| < 60°$ for Egret and $\theta < 10°$ for Fermi as well as for Cosi observations. The coordinates (b, l) denote the galactic latitude and longitude, which are related to the angular distance θ from the GC as $\cos\theta = \cos b \cos l$. The photon signal from such galactic regions over the energy range of interest gets contributions from both the prompt γ-ray emission as well as from various secondary emission processes. We discuss such processes below. As we will see, in several cases, depending on the DM mass and the observation energy ranges, secondary emission signals can dominate over the prompt one.

[4] As mentioned in section 2.1, $\frac{dN}{dE}\Big|_{\rm tot} = \sum_F \frac{\langle\sigma v\rangle_F}{\langle\sigma v\rangle_{\rm tot}} \frac{dN^F}{dE}(m_{\rm DM})$. As long as only DM DM $\to VV \to f\bar{f}f'\bar{f}'$ annihilation dominates, $\langle\sigma v\rangle_F$ and thus $\langle\sigma v\rangle_{\rm tot}$ $(= \sum_F \langle\sigma v\rangle_F)$ are proportional to $g_{S\rm DM}^4$ (eq. (2.2)). Hence, $\frac{dN}{dE}\Big|_{\rm tot}$ is independent on $g_{S\rm DM}$ or $\sin\vartheta$.

JCAP01(2026)038

3.1 Primary signal: prompt γ-ray emission

The photon flux through the prompt emission (averaged over the observation region $\Delta\Omega$) is given by (see e.g. [43, 55]:

$$\frac{d\Phi_{\rm prompt}}{dE_\gamma} = \frac{\langle\sigma v\rangle}{8\pi\, f_\chi\, m^2_{\rm DM}} \left.\frac{dN_\gamma}{dE_\gamma}\right|_{\rm tot} \frac{J_{\Delta\Omega}}{\Delta\Omega}\,, \tag{3.2}$$

where $\langle\sigma v\rangle$ is the total velocity-averaged annihilation cross-section of DM particles and $\left.\frac{dN_\gamma}{dE_\gamma}\right|_{\rm tot}$ is the total photon energy spectrum produced per annihilation of DM particles of mass $m_{\rm DM}$ under a given DM model. The factor f_χ takes the values 1 or 2 depending on whether the DM particle is self-conjugate or not. Since in our considered models the DM is a Dirac fermion, $f_\chi = 2$. As discussed in section 2, the spectrum $\left.\frac{dN_\gamma}{dE_\gamma}\right|_{\rm tot}$ for the DM mass range considered in this work is obtained from `HAZMA2` (with an added energy resolution of 5%). The annihilation J-factor for the ROI $\Delta\Omega$ is defined as usual as:

$$J_{\Delta\Omega} = \int_{\Delta\Omega} d\Omega \int_{\rm l.o.s.} ds\; \rho^2_{\rm DM}(r(s,\theta))\,, \tag{3.3}$$

where s runs along the line-of-sight ($l.o.s.$) (with respect to the observer) at an angular distance θ from the GC.

As an illustration, in figure 2 we show by the red dashed line the prompt γ-ray signal arising from the annihilation of galactic DM particles (of mass $m_{\rm DM} = 100\,{\rm MeV}$). The DM interaction with the SM is assumed to driven by the kinetic-mixing model with $m_V = 3\,m_{\rm DM}$ and total annihilation cross-section $\langle\sigma v\rangle = 2\times10^{-26}\,{\rm cm^3\,s^{-1}}$. Here the photon signal (eq. (3.2)) is estimated from the region $4^\circ < |b| < 20^\circ, |l| < 60^\circ$, similar to the region covered by the COMPTEL observations, but masking $|b| \leq 4^\circ$ (as also considered in the next sub-section for the secondary emissions).

3.2 Secondary signals: Inverse Compton Scatterings, bremsstrahlung and In-flight annihilation

The photon flux corresponding to the secondary emission (averaged over the observation region $\Delta\Omega$) induced by DM annihilation in the Galaxy can be estimated as:

$$\frac{d\Phi_{\rm sec}}{dE_\gamma} = \frac{1}{\Delta\Omega}\int_{\Delta\Omega} d\Omega \left[\frac{1}{E_\gamma}\int_{\rm l.o.s.} ds\; \frac{j_{\rm sec}(E_\gamma, \vec{x}(s,b,l))}{4\pi}\right], \tag{3.4}$$

where $j_{\rm sec}$ is the photon emissivity (at a position $\vec{x}$ in the Galaxy) corresponding to one of the secondary processes: (i) Inverse Compton Scatterings (ICS) on the interstellar radiation fields (ISRF) composed of CMB, infrared (IR) and starlight (SL), (ii) bremsstrahlung on interstellar gas particles and (iii) in-flight annihilation (IfA) of positrons. These emissivities can be expressed as (see e.g. [43]):

$$j_{\rm ICS}(E_\gamma, \vec{x}(s,b,l)) = 2\int_{m_e}^{m_{\rm DM}} dE_e\, \mathcal{P}_{\rm ICS}(E_\gamma, E_e, \vec{x})\, \frac{dn_e}{dE_e}(E_e, \vec{x})\,, \tag{3.5}$$

$$j_{\rm brem}(E_\gamma, \vec{x}(s,b,l)) = 2\int_{m_e}^{m_{\rm DM}} dE_e\, \mathcal{P}_{\rm brem}(E_\gamma, E_e, \vec{x})\, \frac{dn_e}{dE_e}(E_e, \vec{x})\,, \tag{3.6}$$

$$j_{\rm IfA}(E_\gamma, \vec{x}(s,b,l)) = \int_{m_e}^{m_{\rm DM}} dE_e\, \mathcal{P}_{\rm IfA}(E_\gamma, E_e, \vec{x})\, \frac{dn_e}{dE_e}(E_e, \vec{x})\,. \tag{3.7}$$

JCAP01(2026)038

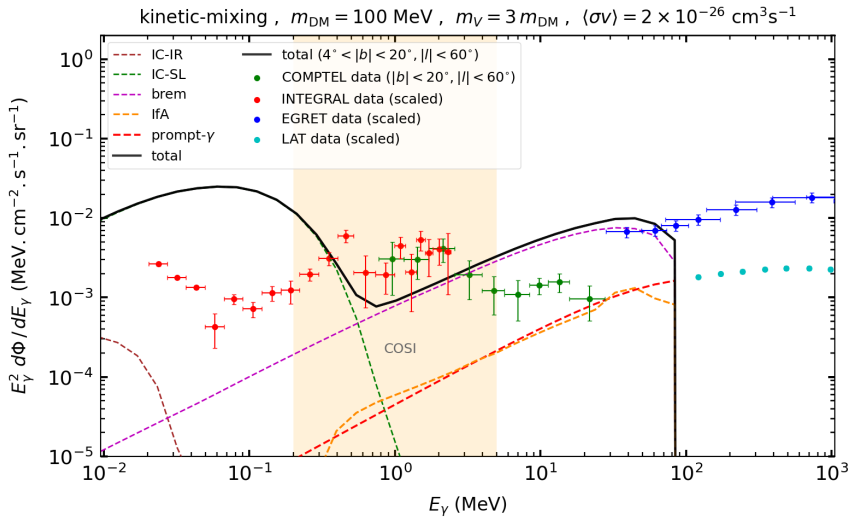

Figure 2. Illustration of the different components (prompt and secondaries) of the *total photon flux* (solid black line) produced due to the annihilation of DM particles (of mass $m_{\rm DM} = 100\,\text{MeV}$) in the Galaxy are shown for the considered photon energy range. The DM interaction is driven by the kinetic-mixing model with $m_V = 3\,m_{\rm DM}$ and the total annihilation cross-section $\langle\sigma v\rangle = 2\times10^{-26}\,\text{cm}^3\,\text{s}^{-1}$. The distribution of DM-induced $e^\pm$ (that give rise to the secondaries) in the Galaxy is obtained considering the approach discussed in section 3.2.1. All DM signals (including the total one) are estimated from the region $4^\circ < |b| < 20^\circ, |l| < 60^\circ$, a region similar to the one covered by COMPTEL observation, but masking $|b| \leq 4^\circ$. The red, green, blue and cyan data points are from the observations of INTEGRAL ($|b| < 15^\circ, |l| < 30^\circ$), COMPTEL ($|b| < 20^\circ, |l| < 60^\circ$), EGRET ($|b| < 10^\circ, |l| < 60^\circ$) and FERMI-LAT ($\theta < 10^\circ$), respectively (as discussed in section 5). All data presented in the figure are rescaled to the observation region of COMPTEL. The light orange band indicates the energy range covered by upcoming MeV telescope COSI (see section 5.3).

Here $\mathcal{P}_{\rm ICS}$, $\mathcal{P}_{\rm brem}$ and $\mathcal{P}_{\rm IfA}$ denote the powers emitted (per photon energy) in the relevant secondary processes into photons with energy E_γ by an e^+ or e^- (having an energy E_e); they are given for reference in appendix A. The function $\frac{dn_e}{dE_e}(E_e, \vec{x})$ in eqs. (3.5)–(3.7) denotes the differential number density distribution of the $e^\pm$ arising due to the DM annihilation.[5] Note that the factor of 2 in (3.5) and (3.6) takes into account the contributions of both the population of positrons and electrons induced by the DM annihilation.

The distribution $\frac{dn_e}{dE_e}$ results due to the injection of the $e^\pm$'s by DM annihilation in a given model. The rate of such injection can be quantified in terms of the source function as:

$$Q_e(E_e^S, r) = \frac{\langle\sigma v\rangle}{2\, f_\chi\, m_{\rm DM}^2} \left.\frac{dN_e}{dE_e^S}\right|_{\rm tot} \rho_{\rm DM}^2(r)\,, \tag{3.8}$$

with $f_\chi = 2$ (for Dirac fermion DM). Here $\left.\frac{dN_e}{dE_e^S}\right|_{\rm tot}$ is the total energy spectrum of $e^\pm$ sourced by the annihilation of DM of mass $m_{\rm DM}$ in a given model. Such a spectrum is obtained using `HAZMA2` (with an added energy resolution of 5%), as discussed in section 2.

[5] For the spatial integral in eq. (3.4), we cut the distribution $\frac{dn_e}{dE_e}(E_e, \vec{x})$ in the radial direction at $R = R_{\rm Gal} = 20\,\text{kpc}$, and in the vertical direction at $|z| = L_{\rm Gal} = 4\,\text{kpc}$, assuming this to be the size of the zone that keeps the $e^\pm$ confined.

JCAP01(2026)038

3.2.1 Semi-analytic approach to obtain the $e^{\pm}$ distribution

The electrons and positrons, after being produced from the DM annihilation, propagate through the galactic medium undergoing several phenomena including spatial diffusion and radiative energy losses and give rise to a steady state distribution. We will be interested in observing the photon signals from the regions around the GC where the effect of energy losses are expected to dominate over other processes. In such a case, the spatial and energy distribution of the steady state $e^{\pm}$'s can be obtained in a semi-analytic way as (see e.g. [55, 56]):

$$\frac{dn_e}{dE_e}(E_e, \vec{x}) = \frac{1}{b_{\rm tot}(E_e, \vec{x})} \int_{E_e}^{m_{\rm DM}} dE_e^S \, Q_e(E_e^S, r) \,, \tag{3.9}$$

where $b_{\rm tot}(E_e, \vec{x})$ denotes the total energy loss rate of the $e^{\pm}$ in the galactic medium via various processes. These (in order of importance with increasing $e^{\pm}$ energy) are: Coulomb interactions with the interstellar gases, ionization of the same gases, bremsstrahlung on the same gases, synchrotron emission in the galactic magnetic field and ICS off the ambient photons in the ISRF. See [57] for the detailed expressions of these energy losses. The maps for galactic gases, ISRF photons and magnetic field are obtained from [57] and are same as the ones used in [20, 21] as well as in [55].

In this semi-analytic approach, in order to be on the conservative side, we estimate the DM-induced secondary (eq. (3.4)) as well as the primary (eq. (3.2)) photon signals from a region $|b| > 4^\circ$, i.e., applying a mask of 4° above and below the Galactic Plane (GP). This process excludes most of the signal that can come from the GP.

In figure 2 we show different secondary photon signals (corresponding to ICS off different ambient photons, bremsstrahlung and in-flight annihilation) produced as a result of the annihilation of galactic DM particles (of mass $m_{\rm DM} = 100\,\text{MeV}$) in the context of the kinetic-mixing model (with $m_V = 3\, m_{\rm DM}$). The DM-induced $e^{\pm}$ distribution that gives rise to such signals are obtained using eq. (3.9). The secondary signals are estimated from the region $4^\circ < |b| < 20^\circ, |l| < 60^\circ$. Figure 2 shows that, in the energy range considered here, the secondary photons can in principle dominate the total DM signal.

3.2.2 Full propagation of $e^{\pm}$ in the Galaxy

We also consider the full galactic propagation of the DM-induced $e^{\pm}$. This involves, apart from the radiative energy losses, various other processes, such as spatial diffusion, advection, convection and re-acceleration. The final distribution ($\frac{dn_e}{dE_e}(E_e, \vec{x})$) resulting after all such processes can be obtained by solving a differential equation representing the transport or propagation of $e^{\pm}$; see e.g. eq. 2.1 of [58] and [59]. We solve such an equation using the numerical package `DRAGON2` [58, 59], considering two Galactic propagation models, named here as 'prop. a' and 'prop. b'. These models were used in [60] as baseline models for the study related to the secondary photon emissions from astrophysical origins towards the GC. Such galactic emissions were later used in [61] as fiducial photon backgrounds in the context of the upcoming MeV telescopes such as Cosi.

Model 'prop. a'. It refers to the propagation model 'DRELowV' from [60], where the spatial diffusion is parameterized as a function of the propagating particle rigidity (R) as

JCAP01(2026)038

$D(R) = D_0\,\beta_e\,(R/R_0)^\delta$, with β_e as the dimensionless particle velocity. The values of D_0, R_0 and δ are $1.46 \times 10^{29}\,\mathrm{cm^2\,s^{-1}}$, 40 GV and ~ 0.33, respectively. The Alfvén velocity (related to the re-acceleration of the particles) is $v_A = 8.9\,\mathrm{km/s}$. As shown in [60], the secondary fluxes corresponding to this model are similar to that obtained with their other baseline model 'PDDE'.

Model 'prop. b'. We also consider this propagation model which refers to the model 'DRC' from [60]. In this model we have $D_0 = 4.3 \times 10^{28}\,\mathrm{cm^2\,s^{-1}}$, $R_0 = 4\,\mathrm{GV}$, $\delta \simeq 0.395$ and a larger Alfvén velocity $v_A = 28.6\,\mathrm{km/s}$. In addition, it includes a convective wind velocity in terms of its magnitude close to the GP, $v_c = 12.4\,\mathrm{km/s}$, and its gradient perpendicular to the GP, $dv_c/dz = 10.2\,\mathrm{km/s/kpc}$.

In figure 3, we show with black dotted curves the DM-induced total photon signals (prompt + secondaries) in the scenario where the $e^\pm$ distribution that gives rise to the secondaries are obtained considering the full galactic propagation (using the model 'prop. a'). The three panels show the results for three different DM masses, $m_{\rm DM} = 10, 10^2$ and $10^3\,\mathrm{MeV}$, considering the kinetic-mixing model with $m_V = 3\,m_{\rm DM}$ and $\langle\sigma v\rangle = 2 \times 10^{-26}\,\mathrm{cm^3\,s^{-1}}$. Such signals are estimated from the region $|b| < 20°, |l| < 60°$. For each mass, this total signal is compared to that (shown by the black solid line) obtained using the method discussed in section 3.2.1, with a mask $|b| \leq 4°$. As we can see from this figure, in the considered photon energy range, the total photon signals (for different DM masses in the range MeV–GeV) obtained in two different ways can differ at most by a factor of a few. In fact, in some cases, the total signal obtained considering the full propagation of $e^\pm$ remains comparatively stronger. In these cases the propagation phenomena, such as diffusion and re-acceleration, actually help in boosting the secondary signal flux coming from an extended region around the GC. A somewhat similar result was also obtained previously in ref. [23].

Note that in figure 3 we show the effect of considering the galactic propagation of DM induced $e^\pm$ using the propagation model 'prop. a' as an illustration. We discuss the effects of considering both the above-mentioned propagation models in our main results presented in section 6.

4 Cosmic-ray $e^\pm$ flux from sub-GeV DM annihilation in the Galaxy

In this section we move to discuss the electron and positron signals from the annihilation of sub-GeV DM in the Galaxy.

The $e^\pm$'s propagate through the galactic environment and give rise to a contribution to the cosmic-ray flux near the solar system. We estimate such a flux of $e^\pm$ at the location of the Voyager-1 spacecraft and compare it with its data, for the $(e^+ + e^-)$ flux, to derive constraints on our considered DM models. Note that, since Voyager-1 is already outside the solar heliosphere, the effects of solar modulation (which suppresses the flux of low-energy $e^\pm$, as induced by sub-GeV DM) is negligible.

The $e^\pm$ flux mentioned above is estimated (per energy, per area, per time and per solid angle) as: $\Phi_{e^\pm} = \frac{2\,v_e}{4\pi}\,\frac{dn_e}{dE_e}$, where v_e and $\frac{dn_e}{dE_e}$ are, respectively, the velocity and the distribution of $e^\pm$ at the location of Voyager-1 (the factor 2 takes into account the contribution of e^+ and e^-). The distribution $\frac{dn_e}{dE_e}$ is obtained by solving the same propagation/transport

JCAP01(2026)038

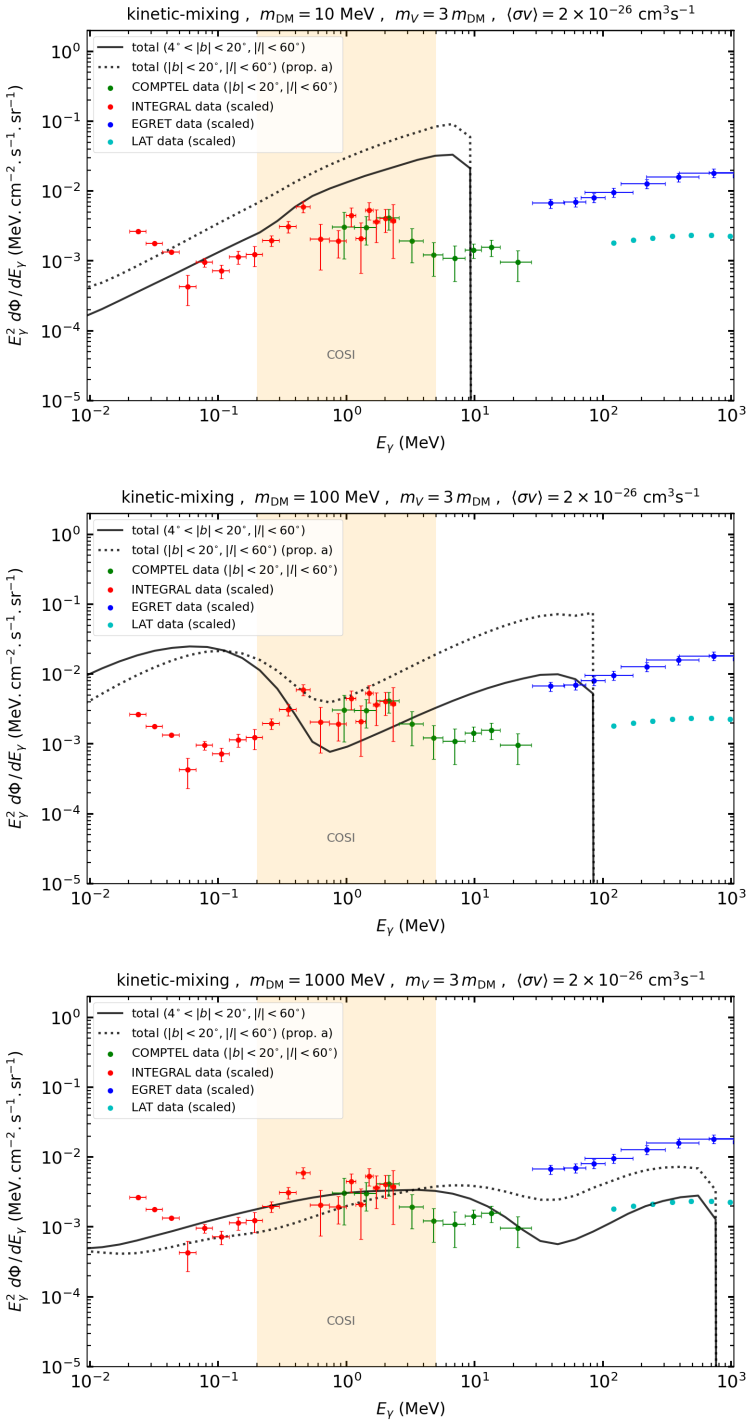

Figure 3. Illustration of the *effects of considering the full propagation* of the DM-induced $e^\pm$ in the Galaxy for three different DM masses: 10, 100 and 1000 MeV. The model is the same one used in figure 2. The galactic propagation of $e^\pm$ is solved numerically using the package `DRAGON2`, with the propagation model 'prop. a' discussed in the text. For each DM mass, the total photon flux obtained (from a region $|b| < 20^\circ, |l| < 60^\circ$) in this way is denoted with a black dotted curve. This flux is compared to that obtained using the method used in figure 2 (the black solid curve), i.e. using the semi-analytic approximated approach for the galactic propagation discussed in section 3.2.1, and masking the region $|b| \leq 4^\circ$.

JCAP01(2026)038

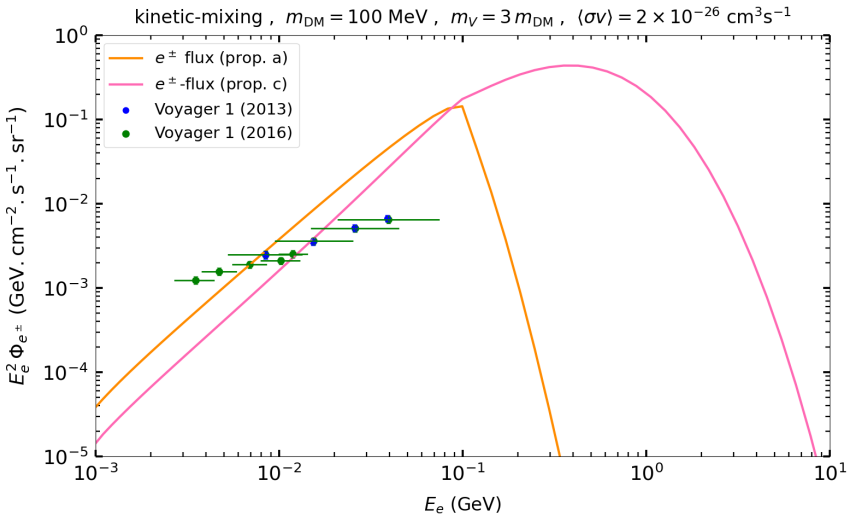

Figure 4. The DM-induced $e^\pm$ *flux* compared to the measurement of VOYAGER-1. The two galactic propagation models 'prop. a' and 'prop. c' discussed in the text are considered. The DM model is the same vector portal one considered in figure 2. The VOYAGER-1 2013 data [17, 62] and VOYAGER-1 2016 data [63] are shown by blue and green points, respectively.

equation mentioned in section 3.2.2 (see eq. 2.1 of [58] and [59]). We again obtain this using `DRAGON2`. For the DM density distribution we use the same profile of eq. (3.1).

We use the model 'prop. a' as described in section 3.2.2. In addition, we also consider another model (named here **'prop. c'**) which refers to the model 'DRE' from [60]. Note that 'prop. c' is almost the same as 'prop. a', the only difference being that the former includes a large Alfvén velocity, $v_A = 42.2\,\text{km/s}$. As shown in [17, 23, 64], such a modification in v_A should have a significant effect on the $e^\pm$ flux at the VOYAGER's location.

In figure 4 we illustrate the resulting DM-induced $e^\pm$ fluxes. These fluxes are shown considering the kinetic-mixing model with $m_{\rm DM} = 100\,\text{MeV}$, $m_V = 3\,m_{\rm DM}$ and $\langle\sigma v\rangle = 2 \times 10^{-26}\,\text{cm}^3\,\text{s}^{-1}$. The VOYAGER-1 data [17, 62, 63] are also shown for comparison. As it can be seen, due to the presence of a higher re-acceleration (corresponding to a larger value of v_A), the model 'prop. c' gives rise to an $e^\pm$ flux that is comparatively more energetic.

5 Data and analysis

We obtain constraints on the sub-GeV DM models by comparing the DM-induced total photon and the cosmic-ray signals (discussed in the previous sections) with the existing X-ray/γ-ray data from INTEGRAL, COMPTEL and FERMI-LAT, and the cosmic-ray $e^\pm$ data from VOYAGER-1, respectively. These observations are briefly presented below.[6]

5.1 Observed data

- INTEGRAL: we use the data from the observations of $\sim 20\,\text{keV}$–$2.4\,\text{MeV}$ photons from the region $|b| < 15°, |l| < 30°$ around the GC. These data, obtained with the SPI

[6] We also considered the γ-ray observations by EGRET, but, since this observation is expected to provide a comparatively weaker constraint on the DM annihilation signal (see, for example, figure 2 or figure 3), we do not discuss it here and henceforth.

JCAP01(2026)038

instrument onboard INTEGRAL, are taken from ref. [65]. For this observation we assume an energy resolution of 0.2% (which is the typical energy resolution of this telescope). We also consider as our fiducial background model the possible diffuse photon flux (discussed in [65]) that arises due to different astrophysical phenomena and can explain this photon observation.

- COMPTEL: we consider the observation of COMPTEL from a region $|b| < 20°, |l| < 60°$. The data, in the photon energy range $\sim 1-15\,\text{MeV}$, are taken from [11, 66]. The energy resolution considered for this telescope is 5% (see, e.g., [44]). We also consider the diffuse astrophysical background photon flux from ref. [16]. This is modeled as a power-law including a super-exponential cutoff, and is in reasonable agreement with the COMPTEL data from a region $|b| < 5°, |l| < 30°$. We scale this diffuse background to the ROI $|b| < 20°, |l| < 60°$ and use as our fiducial background flux. Note that, while the COMPTEL data have not been included in past works such as ref. [20, 21], they actually turn out to be pertinent, albeit in a narrow window of the parameter space.

- FERMI-LAT: we also consider the FERMI-LAT observation from a region of radius 10° around the GC. For our purposes, we use the data in the energy range $100\,\text{MeV} \lesssim E_\gamma \lesssim 1\,\text{GeV}$ provided in [60, 67]. We assume an energy resolution of 7.5% [44].

- VOYAGER1: we consider the data for the $e^+ + e^-$ flux collected by the VOYAGER-1 spacecraft outside the solar heliosphere. These data, corresponding to VOYAGER-1 (2013) over an $e^\pm$ energy range $\sim 8 - 40\,\text{MeV}$ and to VOYAGER-1 (2016) over the range $\sim 3 - 100\,\text{MeV}$, are taken from [17, 62] and [63], respectively. For each DM model, at each DM mass, we consider the strongest bound obtained from either of the two data sets as our VOYAGER-1 limit.

5.2 Analysis with the observed data

We compare different DM signals with the corresponding experimental observations discussed above by taking the following two analysis approaches.

- **Conservative approach**: in this approach we follow a strategy similar to the one used in ref. [11, 17, 56]. We do not assume anything on the astrophysical backgrounds and compare the DM-induced signals directly to the observed data. For each experimental observation with the corresponding data points, we impose the constraint that the annihilation signal from a fixed DM model (for a given DM mass) should not exceed any of the experimental data points at any energy bin by more than 2σ. For example, for each X-ray/γ-ray observation from a particular observation region, we make sure that, for a given DM mass, the DM-induced total photon signal (prompt + secondaries) (discussed in section 3) from that region does not exceed the observed central value plus twice the error bar in any energy bin. Also, in the context of the cosmic-ray $e^\pm$ data observed by VOYAGER-1, we take the same approach to constrain the signal from DM. These lead to upper-limits on the total annihilation cross-section of DM in a given model, which are presented in section 6.

JCAP01(2026)038

◀ **Optimistic approach**: in this alternative approach we assume the observed data to be of some astrophysical origin, and then impose the condition that the DM signal, when added to such astrophysical background, does not exceed the data points. This makes our constraints on DM comparatively stronger. We do this for INTEGRAL and COMPTEL data only, for which we possess a reliable estimate of the background (see section 5.1).[7] We adopt a simple chi-squared statistic:

$$\chi^2 = \sum_i \frac{(\phi_i^0 - \phi_i^{\rm DM}(\langle\sigma v\rangle) - \phi_i^{\rm BG})^2}{\sigma_i^2}\,, \tag{5.1}$$

where ϕ_i^0 is the observed data from a given experiment (at the i-th energy bin) with σ_i representing the corresponding error bar, $\phi_i^{\rm BG}$ is the astrophysical background that fits the corresponding observed data, and $\phi_i^{\rm DM}(\langle\sigma v\rangle)$ is the signal from the annihilation of DM (with a fixed mass) in a given model. For a given experiment, we obtain a 95% C.L. upper-limit on the signal normalization $\langle\sigma v\rangle$ (for a given $m_{\rm DM}$) by requiring that $\Delta\chi^2 = \chi^2 - \chi_0^2 = 2.71$, where χ_0^2 is the best-fit χ^2-value with zero DM signal. In section 6 we present such constraints.

5.3 Upcoming MeV telescope COSI

As we saw in section 3, the photon signals arising from the annihilation of DM particles with masses in the range MeV–GeV populate the energy range $\sim 0.1{-}100\,$MeV, the so called 'MeV gap' [68]. Such a range will be probed by a number of upcoming space-based MeV telescopes, e.g., COSI [69, 70], AMEGO [71, 72], E-ASTROGAM [73, 74], GECCO [75] GRAMS [76], ADEPT [77] and PANGU [78] with sensitivities much better than that of the existing or past telescopes (such as INTEGRAL, COMPTEL and EGRET).

In this work, we focus on the upcoming telescope COSI, which has already been selected to fly. COSI is a space-based wide field-of-view telescope with an operational energy range $0.2{-}5\,$MeV. It employs a compact Compton telescope design and contains several high-purity germanium semiconductor detectors. These help COSI have a high-resolution spectroscopy (with an energy resolution $\lesssim 4\%$), a direct imaging over a wide field-of-view ($\gtrsim 25\%$ of the sky), as well as an effective suppression for the background events. Its effective area and angular resolution are above a few cm^2 and above a few degrees, respectively. With its scheduled launch in 2027, COSI is supposed to start surveying the sky orbiting Earth and will be able to assure a daily full-sky coverage. For an overview of its instrumentation and technical details, see [69, 70].

We estimate the projected sensitivity of COSI on our considered sub-GeV DM models following a methodology similar to the one adopted in [14] (regarding the continuum photon signal from the GC). Note that ref. [14] studied the prospects of COSI for sub-GeV DM annihilation (considering a couple of annihilation channels) based on only the prompt emission. We consider the same target region (as in [14]) of radius 10° around the GC and compare

[7] In the case of the FERMI-LAT GC observation, the modeling of the corresponding photon background is quite uncertain (see e.g. [60]) and subject of intense investigations in itself so that entering in the details would go beyond our scope. The VOYAGER-1 observations also exhibit a relatively large uncertainty in the corresponding background modeling (see e.g. [17]).

JCAP01(2026)038

the DM-induced total photon signal composed of prompt and secondary emissions from this region with the COSI sensitivity, in order to estimate the projection on the corresponding DM annihilation rate. The 3σ projected sensitivity of COSI corresponding to the continuum emission is obtained from figure 4 of ref. [61]. This COSI sensitivity (for a 2 yrs of mission time), provided for a disk-like observation region with 20° radius around the GC, is then rescaled to our observation region following the prescription given in [61] (as also used in [14]). Knowing that such sensitivity scales as the squared root of the observation time, we obtain the COSI sensitivity for a mission time of 4 yrs (which corresponds to approximately 1 yr of observation time, see [61]). Note that the minimal, nominal mission lifetime of COSI is 2 years, but a longer duration is likely. We then obtain the projected sensitivity on the total DM annihilation rate for a given DM mass and a given model by ensuring that the corresponding total DM signal overcomes the 3σ COSI sensitivity at least in one of the five energy bins for which the sensitivity is provided in ref. [61]. The projections obtained in this way are presented in section 6.

6 Results and discussion

6.1 Constraints from existing data

In this section we present the indirect detection constraints obtained on the two considered sub-GeV DM models based on existing astrophysical data and the two approaches discussed in section 5. These constraints are shown on the total annihilation cross-section $\langle\sigma v\rangle$ as a function of $m_{\rm DM}$ in the range 1 MeV–1 GeV.

Figure 5 shows the results for the kinetic-mixing and higgs-portal models in the left and right panels, respectively. In the top row of the figure, the red, green and cyan curves show the constraints obtained on the two models from X-ray/γ-ray observations of INTEGRAL, COMPTEL and FERMI-LAT, respectively. The total photon signal is obtained using the method described in section 3.2.1, with a mask $|b| \leq 4°$. In each case, the constraint shown by the solid curve is obtained under the conservative analysis described in section 5.2, i.e., comparing the DM signal directly with the observed data without making any assumption on the astrophysical background. The strong INTEGRAL limit between ~ 30 MeV and 1 GeV is a consequence of a strong secondary signal, in particular the one produced via the ICS of the DM-induced $e^{\pm}$ off the optical starlight, at an energy where the intensity of the INTEGRAL data is at a minimum (see figures 2 and 3 for an illustration). For $m_{\rm DM} \gtrsim 50$ MeV, INTEGRAL typically provides the dominating constraint on sub-GeV DM among different photon observations based on mainly such ICS signals. For the higgs-portal case, the FERMI-LAT constraint becomes marginally stronger for $m_{\rm DM} > 600$ MeV. For $m_{\rm DM}$ below ~ 30 MeV, the ICS signal falls below the INTEGRAL energy range, and thus the corresponding INTEGRAL constraint is driven by the signals resulting from bremsstrahlung, prompt emission and in-flight annihilation. COMPTEL provides a better constraint in the mass range from a few MeV to ~ 60 MeV, based on mainly bremsstrahlung, prompt emission and in-flight annihilation. Below this mass range INTEGRAL dominates again. The plunge in the INTEGRAL/COMPTEL limit in the higgs-portal case for $m_{\rm DM}$ below the electron mass threshold (i.e., $m_{\rm DM} < 2$ MeV) results due to the photon line signals appearing from the decay of the mediator S into prompt γ's (which is the dominating decay mode of S for these DM masses).

JCAP01(2026)038

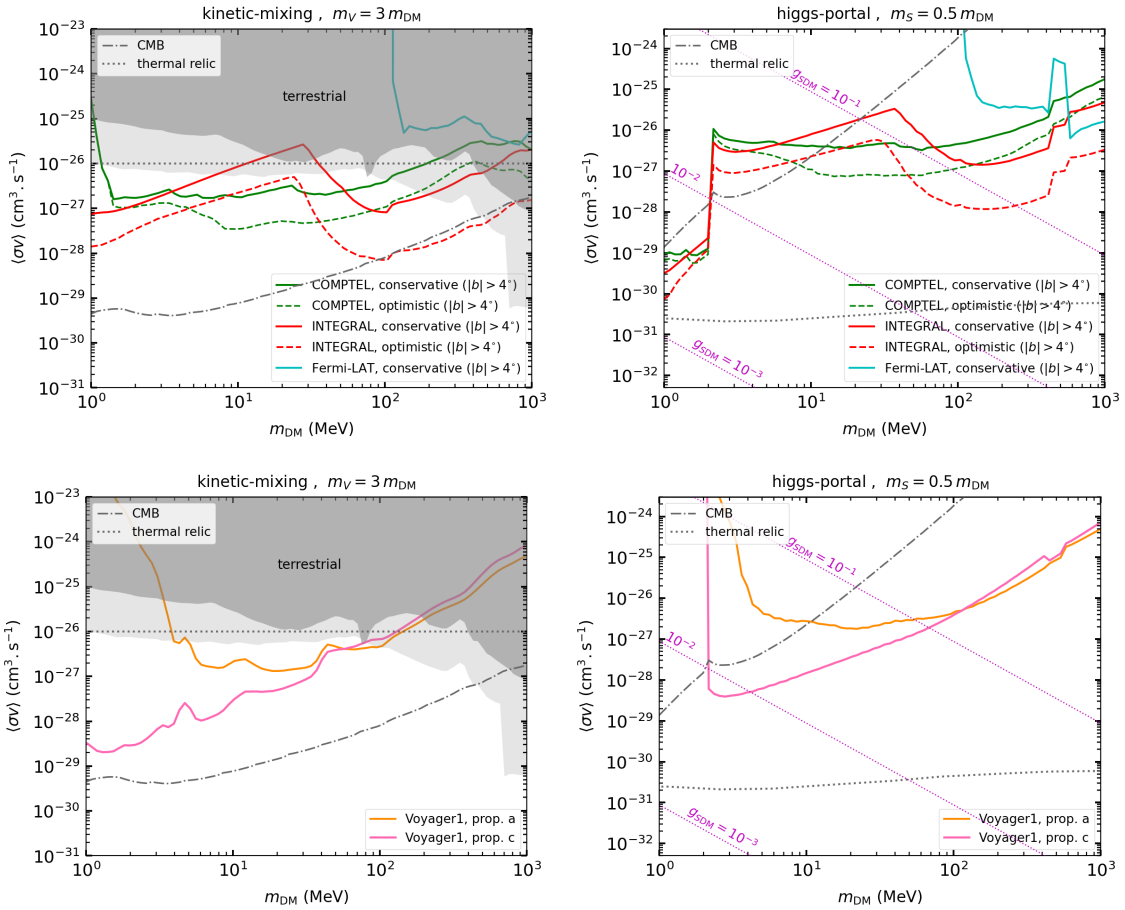

Figure 5. *Indirect detection upper-limits* obtained on the total $\langle\sigma v\rangle$ of the two considered DM models (vector portal and scalar portal, left and right panels respectively) based on existing astrophysical observations. Limits obtained by comparing the DM-induced total photon signal (primary + secondaries) with data from COMPTEL, INTEGRAL and FERMI-LAT are presented in the upper panels by green, red and cyan curves, respectively. The solid curves are obtained under the conservative analysis, while the dashed curves are obtained using the optimistic analysis. Limits obtained by comparing the DM-induced $e^{\pm}$ flux with VOYAGER-1 data (under the conservative analysis) are shown in the lower panels by the orange and pink solid curves, which correspond to the galactic propagation models 'prop. a' and 'prop. c', respectively (see the text). We also show the thermal relic DM line (gray dotted lines) and the CMB bounds (gray dashed-dotted lines), as well as the combined exclusions (dark gray region) and the combined projections (light gray region) from terrestrial experiments [51]. The contours corresponding to different values of the coupling $g_{S\rm DM}$ are indicated by the purple dotted lines on the right.

In figure 5 the constraints shown by the colored *dashed* curves (for INTEGRAL and COMPTEL) are obtained using the optimistic analysis taking into account the standard photon backgrounds mentioned in section 5. Adopting this approach, the bounds are improved significantly, by an amount that depends on the $m_{\rm DM}$ value. For example, in the case of INTEGRAL, this improvement is an order of magnitude for $m_{\rm DM} \gtrsim 80\,\text{MeV}$. Due to this, it is possible to constrain the parameter space of the kinetic-mixing/higgs-portal model down to $\langle\sigma v\rangle \simeq 10^{-28}\,\text{cm}^3/\text{s}$ for a DM mass of $\sim 100\,\text{MeV}$.

JCAP01(2026)038

In the lower row of figure 5 we present the exclusion limits obtained on the kinetic-mixing and higgs-portal models from VOYAGER-1 data. The orange and pink curves show the limits obtained considering the two galactic propagation models 'prop. a' and 'prop. c' (mentioned in sections 3 and 4), respectively. For DM masses below $\sim 50\,\mathrm{MeV}$, model 'prop. c' leads to a much stronger constraint compared to that obtained with model 'prop. a'. As noted in section 4, since 'prop. c' includes a larger re-acceleration velocity (v_A), for a given $m_{\rm DM}$ this model gives rise to a much more energetic cosmic-ray flux of $e^{\pm}$ compared to that obtained with model 'prop. a'. As a result, the soft $e^{\pm}$ spectra induced by a low mass DM get boosted in energy after the propagation and fall in the energy range of VOYAGER-1, leading to a stronger constraint on that DM mass. Based on such effects, using VOYAGER-1 data one can exclude $\langle\sigma v\rangle$ for both models down to $\sim 10^{-28}\,\mathrm{cm}^3/\mathrm{s}$ for a DM mass of $\sim 10\,\mathrm{MeV}$. For the higgs-portal model, since $m_S = m_{\rm DM}/2$ in our setup, the VOYAGER-1 limits evaporate for $m_{\rm DM} < 2\,\mathrm{MeV}$ due to the closing of all leptonic annihilation channel including e^+e^-.

In figure 6, we show the combined upper-limits from different existing X-ray/γ-ray observations with the black solid curves (corresponding to the conservative approach), together with the bounds from VOYAGER-1 in pink curves (corresponding to the propagation model 'prop. c'). As we can see, for both DM models, the existing photon observations provide better constraints compared to those coming from VOYAGER-1 for $m_{\rm DM} \gtrsim$ a few tens of MeV. Below this mass range, VOYAGER-1 usually provides a better constraint (except for the higgs-portal case with $m_{\rm DM} \lesssim 2\,\mathrm{MeV}$) depending on the choice of the propagation model.

6.2 Projected sensitivity of COSI

In this section we discuss the projected sensitivities of the upcoming MeV telescope COSI in probing the sub-GeV DM models based on the approach described in section 5.3. In figure 6 we show with brown curves these COSI sensitivities (at 3σ) in the usual $\langle\sigma v\rangle - m_{\rm DM}$ plane for kinetic-mixing (left panel) and higgs-portal (right panel) models. As mentioned in section 5.3, such sensitivities are obtained considering 1 year of COSI observation towards a 10° disk region around the GC.

The brown solid curves in figure 6 correspond to the projections obtained using the total photon signals estimated following section 3.2.1 with a mask $|b| \leq 4^\circ$. The brown dotted and dashed curves, on the other hand, show the projections obtained with the photon signals estimated considering the effect of galactic propagation of DM-induced $e^{\pm}$, under the models 'prop. a' and 'prop. b', respectively (discussed in section 3.2.2). As pointed out in sections 3.2.1 and 3.2.2, the cases with propagation can actually produce a larger flux for the total photon signal over the energy range of interest, especially for $m_{\rm DM}$ below a few hundreds of MeV. As a result, in this mass range, the COSI projections are comparatively stronger. Model 'prop. b', in spite of including the convection of $e^{\pm}$, provides a stronger projection (especially for $m_{\rm DM}$ between a few MeV and $\sim 200\,\mathrm{MeV}$) due to its lower value for the diffusion coefficient and a larger value for the re-acceleration velocity (see section 3.2.2). We recall from section 5.3 that these propagation models were used in ref. [60] as baseline models for studying the secondary photon emissions from astrophysical processes towards the GC. Such galactic emissions were then used in ref. [61] as fiducial backgrounds while estimating the COSI sensitivity (which is considered in the present work). Hence this ensures consistency between out treatment of the signal and of the background, for these cases.

JCAP01(2026)038

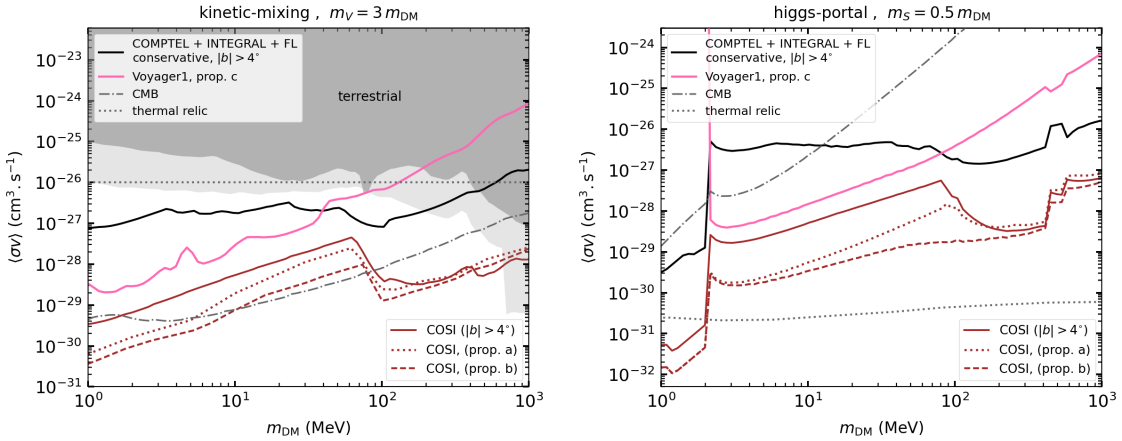

Figure 6. *Summary of the constraints* on the kinetic-mixing model (left panel) and the higgs-portal model (right panel) as well as 3σ *projected sensitivities* of the upcoming MeV telescope COSI (for an observation time of 1 year). The latter ones are shown by the brown curves. The brown solid curves are the projections where total photon signal is obtained using the method described in section 3.2.1 (with a mask $|b| \leq 4^\circ$). The effects of considering the full Galactic propagation of $e^\pm$ are shown by the brown dotted (dashed) curves which correspond to the propagation model 'prop. a' ('prop. b') discussed in section 3.2.2.

Like in the case of the X-ray/γ-ray upper-limits discussed above, the strengthening in the COSI projections around $\sim 100\,\text{MeV}$ and above is due to the excess of the ICS signal produced by the scattering of DM-induced $e^\pm$ off the optical starlight, at an energy where the sensitivity of COSI is stronger [61]. I.e., for $m_{\rm DM} \gtrsim 100\,\text{MeV}$ the COSI sensitivity is driven mainly by the ICS signal, while for $m_{\rm DM} < 100\,\text{MeV}$ the main photon signal is a combination of bremsstrahlung, in-flight annihilation and prompt emission. For the higgs-portal model, the plunge in the projections for $m_{\rm DM}$ below the electron threshold ($m_{\rm DM} < 2\,\text{MeV}$) appears due to the photon line signals produced from the decay of the mediator. Also, note that the visible features at higher DM masses for both the models correspond to the muon and pion thresholds.

As can be seen from figure 6, for both the sub-GeV DM models, the upcoming COSI observations will be able to probe a vast region of the parameter space that lies beyond the constraints placed by the existing X-ray, γ-ray and cosmic-ray data. For example, for the kinetic-mixing model, COSI is sensitive to such values of $\langle\sigma v\rangle$ that are at least an order of magnitude below the combined bound set by existing indirect searches for $m_{\rm DM} \lesssim 40\,\text{MeV}$ and $m_{\rm DM} \gtrsim 80\,\text{MeV}$. For the higgs-portal model, such improvements vary from a factor of few to one/two orders of magnitude, depending on the choice of propagation parameters used for the estimates related to COSI.

6.3 Importance of secondary photons

An important ingredient of the present work consists in constraining or probing sub-GeV DM based on signals that includes different secondary emissions produced by DM-induced $e^\pm$ in the Galaxy. To stress this point, in figure 7 we illustrate the importance of including such secondary emissions for the two considered sub-GeV DM models. For each model, the solid

JCAP01(2026)038

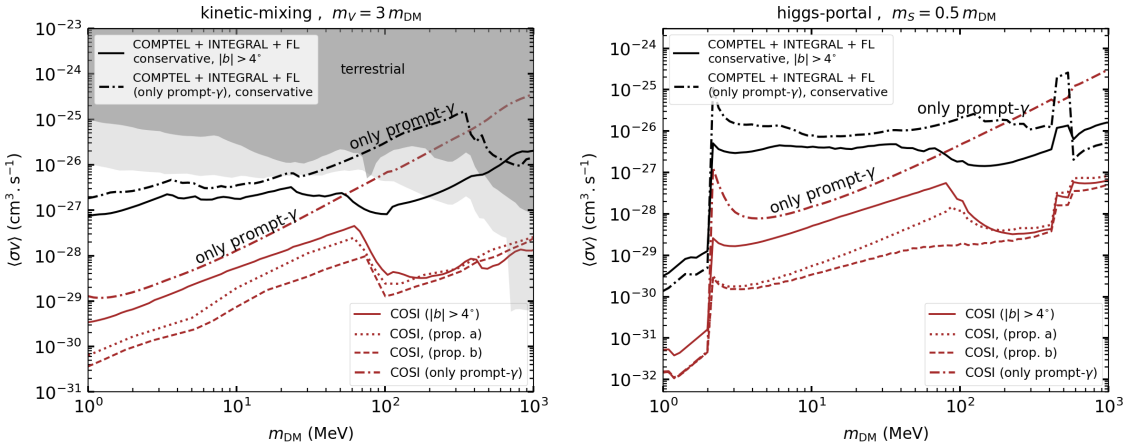

Figure 7. *Importance of the inclusion of secondary photons.* The combined conservative bounds and the COSI projections are shown with and without including the secondaries, considering the kinetic-mixing (left panel) and the higgs-portal (right panel) models. The dashed-dotted black and brown curves correspond to the case neglecting the secondary photon signals, while the other black and brown curves show the results obtained including the secondaries and are same as the ones presented in figure 6.

black line in figure 7 corresponds to the combined bound (obtained with the conservative approach) from existing X-ray/γ-ray observations and is the same as the one shown in figure 6. The black dashed-dotted line, on the other hand, corresponds to the bound obtained by switching off all the secondary emissions and considering only the prompt γ-ray emission (without the mask $|b| \leq 4^\circ$). As it can be seen, the bounds including the secondaries are stronger for almost all the DM mass range, although the effect is much more prominent in the mass range $\sim 50-600\,\text{MeV}$ where the improvement can be of one order of magnitude. Indeed, in this mass range, the total signal is driven mainly by the ICS signal. For completeness, we also notice that, for some DM masses e.g. close to 1 GeV, the limits obtained considering both prompt and secondary photon signals turn out to be weaker compared to those obtained using only prompt γ-ray signal. This is mainly due to the fact that, in the former case as mentioned in section 3.2.1, we remove all the signals (both prompt and secondaries) coming from a 4° region above and below the GP (to be on the conservative side), while in later case the prompt signal from this region is included in the analysis.

The effect of considering the secondaries is much more significant for the COSI projections, as can be seen by comparing the brown dashed-dotted lines which do not include secondaries with the other brown lines which include secondaries and are the same as the ones shown in figure 6. Again the significance of secondaries turns out to be more important for higher DM masses (in particular for $m_{\rm DM} \gtrsim 100\,\text{MeV}$) where the improvement can be significantly large, up to a few orders of magnitude. For example, for the kinetic-mixing model, at $m_{\rm DM} \simeq 500\,\text{MeV}$, the projection obtained including secondaries (with a mask $|b| \leq 4^\circ$) is almost three orders of magnitude stronger than that obtained without secondaries (without the mask $|b| \leq 4^\circ$). As mentioned above, such an improvement relies mainly on the inclusion of the ICS signal. Note that, for some DM masses, the projections based on the total photon

JCAP01(2026)038

signal can be weaker compared to that obtained with only prompt emission (see, e.g., the higgs-portal case for $m_{\rm DM} < 2\,{\rm MeV}$) due to the same reason mentioned above in the case of the existing photon observations.

6.4 Comparison with other constraints

6.4.1 Thermal freeze-out relic DM

Although this work does not require specifically a thermal freeze-out relic DM scenario, we show, just for the sake of comparison, in each plot of the $\langle\sigma v\rangle - m_{\rm DM}$ plane the contour (by the gray dotted line) that yields the correct DM relic density [79] under the standard thermal freeze-out scenario. For the kinetic-mixing model, where the DM annihilation proceeds through s-wave, this $\langle\sigma v\rangle$ for the thermal relic DM is taken to be $\langle\sigma v\rangle \simeq 10^{-26}\,{\rm cm^3\,s^{-1}}$ [24, 25, 80]. For the higgs-portal model (where the DM annihilation proceeds through p-wave) this $\langle\sigma v\rangle$ is of the order of $10^{-31}\,{\rm cm^3\,s^{-1}}$ [24, 25].

As we can see from figure 5 (or 6), for the kinetic-mixing model, the combined indirect search bounds from existing observations already rule out the standard thermal relic sub-GeV DM scenario for $m_{\rm DM}$ up to $\sim 800\,{\rm MeV}$. As the present work shows, the upcoming instrument COSI is expected to provide a further strong constraint on this parameter space. Note that there are mechanisms for producing the observed DM through different non-standard processes which can be considered to open up the parameter space for the sub-GeV DM candidates considered here; see for example [81–83] for detailed discussions.

For the higgs-portal model, as it can be seen from figure 5 (or 6), the present indirect detection constraints on $\langle\sigma v\rangle$ are weaker compared to the standard thermal relic value. The upcoming COSI is expected to probe this thermal relic value only for $m_{\rm DM} \lesssim 2\,{\rm MeV}$. Note that, in this kind of scenario, the value of $\langle\sigma v\rangle$ that corresponds to the observed relic density can become significantly larger than the standard one shown here by considering a modified cosmological setup; see for example [84].

We also note that, considering a Dirac fermion DM under the standard thermal scenario, Big Bang Nucleosynthesis (BBN) constrains the DM mass below a few MeV; see [85, 86] and [36].

6.4.2 CMB constraints

In each $\langle\sigma v\rangle - m_{\rm DM}$ plane we show the constraint from Planck CMB observation [79] with a gray dash-dotted line. This is estimated for the two considered sub-GeV DM models (where DM is a Dirac fermion with particle-antiparticle symmetry) following [44] with the efficiency factors for $e^{\pm}$ and γ from [87]. The CMB constraint for the kinetic-mixing model is comparatively much stronger (compared to the thermal line) since here the DM annihilation is s-wave. On the other hand, this constraint in the case of the higgs-portal model is much weaker since here the annihilation is p-wave. In this case, the DM velocity at recombination which is required to translate the CMB constraint on $\langle\sigma v\rangle$ to its present-day value is estimated considering an optimistic choice for the kinetic decoupling temperature of $x_{kd} = 10^{-6}$ (increasing which should relax the CMB constraint) [11]. Note here that, in the cases in which the vector portal model also features p-wave annihilations (e.g. if the DM is a complex scalar or a Majorana fermion), the CMB constraints are equally relaxed and the

JCAP01(2026)038

corresponding thermal relic lines go down. Instead the indirect detection limits obtained in our analysis are sensitive only to DM annihilation at the present time and therefore are quite independent of the s-wave/p-wave assumption if we consider, as usually done, a constant DM speed in the galactic halo.

We see from figure 5 (or 6) that, for the kinetic-mixing model, the indirect detection constraints derived using existing data are weaker compared to the bound from the CMB. Taking an optimistic approach using the standard astrophysical backgrounds for the photon observations, this comparison can be improved. For example, the optimistic bound from INTEGRAL reaches at the same level of the CMB bound for $m_{\rm DM}$ in the ranges $\sim 100\,\text{MeV}$–$1\,\text{GeV}$. On the other hand, as can be seen from figure 6, the upcoming COSI (with a year of observation towards the GC) can in principle improve the situation a lot by providing a good sensitivity to the secondary emissions produced from the DM annihilation under this model. For example, it can probe values of $\langle\sigma v\rangle$ that lie almost an order of magnitude below the CMB bound for $m_{\rm DM} \gtrsim 100\,\text{MeV}$. Considering the effects of a full galactic propagation of DM-induced $e^{\pm}$ on the corresponding secondary emissions, such COSI projections can be improved even further, especially below $m_{\rm DM} \simeq 70\,\text{MeV}$, by reaching at the same level of the CMB bound or becoming stronger than this.

The situation is quite different in the case of the higgs-portal model. Figure 6 (or 5) shows that, for this model, the combined indirect search bounds from X-ray, γ-ray and cosmic-ray observations (even the ones obtained with the conservative approach) are much stronger than the CMB bound for almost the entire DM mass range MeV-GeV, especially for $m_{\rm DM} \gtrsim 10\,\text{MeV}$. The upcoming COSI (with a year of observation towards the GC) then will be able to probe for this model much deeper into the parameter space that lies several orders of magnitude below the CMB bound in the whole DM mass range $1\,\text{MeV}$–$1\,\text{GeV}$.

Note that the CMB constraint discussed above can be evaded independently for example in a scenario where the DM is partially produced from the decay of a heavier dark-sector particle after recombination; see [88]. On the other hand, the indirect detection bounds or projections derived here remain unaltered in such a scenario.

6.4.3 Terrestrial constraints

For the kinetic-mixing model, we also compare our results with the combined exclusions and the future projections from different terrestrial experiments. These exclusions and projections, obtained from figure 3 of [51] for the masses we are interested in, are shown in figures 5, 6 and 7 by the dark and light gray shaded regions, respectively. For the projected sensitivities, we consider the future experiments that are starting their operations or have secured full funding. These terrestrial exclusions and projections are shown originally in the $y - m_{\rm DM}$ plane (with the quantity y defined in eq. (2.1)), along with the contours corresponding to the observed relic density obtained under the thermal freeze-out scenario for different DM candidates (see also [42, 50]). Since the total pair-annihilation cross-section ($\langle\sigma v\rangle$) of DM into SM for a given $m_{\rm DM}$ is proportional to y (as shown in eq. (2.1)), and considering that $\langle\sigma v\rangle_{\rm thermal} \simeq 10^{-26}\,\text{cm}^3\,\text{s}^{-1}$ for the correct thermal relic density for DM, we convert the experimental constraints and projections from $y - m_{\rm DM}$ plane to the $\langle\sigma v\rangle - m_{\rm DM}$ plane using the relation $\langle\sigma v\rangle_{\rm exp} = \langle\sigma v\rangle_{\rm thermal} \times (y_{\rm exp}/y_{\rm thermal})$. The quantity $y_{\rm thermal}$, indicating

JCAP01(2026)038

the thermal relic contour, corresponds to the case of a Majorana DM with a multiplication factor of 2 (since our DM is a Dirac fermion with particle-antiparticle symmetry). Note that these terrestrial constraints and projections are shown for a choice of the coupling parameter $\alpha_D = g^2_{V\mathrm{DM}}/4\pi = 0.5$ used in most of the literatures. Assuming a smaller value of α_D will strengthen these combined constraints and projections; see, e.g., [42] for a quantitative discussion. On the other hand, as mentioned in section 2.1, since the DM-induced photon and $e^{\pm}$ spectra in this model (for the masses we are interested) do not depend on α_D, the indirect detection limits on $\langle\sigma v\rangle$ remain unaffected under the variation of this parameter.

Figures 5 and 6 show that, for the kinetic-mixing model, our combined indirect detection constraints (based on prompt and secondary photon signals) from existing X-ray + γ-ray observations as well as from Voyager-1 observation, obtained with the conservative approach (without assuming any background modeling), provide better exclusions than those from existing terrestrial experiments for a DM mass up to $\sim 450\,\mathrm{MeV}$. In this mass range, these indirect detection bounds are stronger then the terrestrial ones by more than 1–2 orders of magnitude depending on m_{DM}. Such constraints also exceed the projected sensitivities of upcoming terrestrial experiments for a DM mass up to $\sim 200\,\mathrm{MeV}$. Taking an optimistic approach using the standard astrophysical backgrounds, such indirect detection bounds are improved by an order of magnitude and the above-mentioned mass ranges are extended up to $\sim 800\,\mathrm{MeV}$ and $\sim 500\,\mathrm{MeV}$, respectively.

From figure 6 we see that the upcoming MeV telescope Cosi will be able to explore a much larger region of the parameter space of the kinetic-mixing model, thanks to the significant leverage provided by its sensitivity to secondary emissions. With a year of observation towards the GC, Cosi will be able to probe a vast parameter space that lies *well beyond* the reach of the present or future terrestrial experiments for a DM mass range that is extended up to $\sim 600\,\mathrm{MeV}$. Hence it can complement these terrestrial experiments in the search for sub-GeV DM signals in this mass range.

For the higgs-portal model with $m_S < m_{\mathrm{DM}}$, the DM pair-annihilation cross-section depends only on the coupling $g_{S\mathrm{DM}}$, but not on the the mixing parameter $\sin\vartheta$ between the scalar mediator and the SM higgs. The only requirement is that there is some value of $\sin\vartheta$ consistent with the terrestrial observations, and that it is large enough that the decay length of the mediator is below the parsec scale [24]. Hence, the complementarity between the indirect detection constraints and those from the terrestrial searches [39] can not be shown in the $\langle\sigma v\rangle - m_{\mathrm{DM}}$ plane. For this model, we compare our results with the cosmological constraints (CMB and relic abundance). In addition, like in [24], we show (in figure 5) some contours of constant $g_{S\mathrm{DM}}$ to get an idea of reasonable values of $\langle\sigma v\rangle$. For example, the existing photon and cosmic-ray observations together are able to constrain the values of $g_{S\mathrm{DM}}$ between ~ 0.1 — a few $\times 10^{-3}$ for a DM mass up to a few hundreds of MeV. The near-future Cosi will be able to improve this situation further.

6.4.4 SN1987A constraints

For the kinetic-mixing model, we also compare our DM indirect detection results with the Supernova 1987A (SN1987A) constraints on the same model from [89]. Considering the fiducial SN model and a choice for the coupling parameter $\alpha_D = 0.5$ (like in the case of the terrestrial constraints discussed above), we map the region of the parameter space excluded

JCAP01(2026)038

by SN1987A from the $y - m_{\rm DM}$ plane (presented in the right panel of figure 6 of [89]) into our $\langle\sigma v\rangle - m_{\rm DM}$ plane (following the same prescription discussed above in section 6.4.3). We find that this excludes a region $10^{-37}\,{\rm cm}^3\,{\rm s}^{-1} \lesssim \langle\sigma v\rangle \lesssim 10^{-31}\,{\rm cm}^3\,{\rm s}^{-1}$ (which falls below the level shown in figure 5 or 6) for $m_{\rm DM}$ in the range 1–$\sim$100 MeV, leaving the other parts of the parameter space, in particular those to be probed by upcoming DM indirect detection searches, allowed.

7 Conclusions

In this work we perform a detailed study of the indirect searches of sub-GeV DM particles (in the MeV–GeV mass range) in two representative realistic models, namely, the vector portal kinetic-mixing model and the higgs-portal model, based on the primary and secondary photon signals as well as the cosmic-ray signals produced in the Galaxy from the pair-annihilation of these DM particles. These models lead to the annihilation of DM particles into realistic final states including various light hadronic resonances. Regarding the photon observations, focusing on different observation regions centered around the GC, we include DM annihilation induced all possible secondary signals that result from Inverse Compton Scatterings (ICS), bremsstrahlung and In-flight positron annihilation (IfA). We adopt standard assumptions for the galactic environment and proper treatments for the galactic propagation of DM-induced $e^{\pm}$ that give rise to the secondary photons as well as the cosmic-ray signals. Based on the above-mentioned signals, we derive indirect detection constraints on the two considered sub-GeV DM models using existing X-ray/soft γ-ray data from experiments like INTEGRAL, COMPTEL and FERMI-LAT and $e^{\pm}$ data from VOYAGER-1. In parallel, we evaluate the projected sensitivity of the upcoming MeV telescope COSI (which is already selected to fly) in probing the parameter space of these DM models, based on all possible primary and secondary photon signals. We compare our indirect detection bounds and projections with other constraints/projections from cosmological observations and different terrestrial experiments.

We find that, thanks to the inclusion of secondary photons, our combined bound on the total DM annihilation rate $\langle\sigma v\rangle$ from existing X-ray and γ-ray observations turn out to be significantly stronger compared to the terrestrial constraints and future projections for a DM mass up to a few hundreds of MeV for the kinetic-mixing model. With a rather optimistic approach using the standard astrophysical backgrounds such bound on this model can reach at the level of the CMB constraint (which is expected to be the dominating constraint for this DM model) for $m_{\rm DM} \gtrsim 100$ MeV, based on mainly the ICS signal. For the higgs-portal model, on the other hand, this combined bound overcomes the CMB constraint by one to several orders of magnitude for $m_{\rm DM}$ above ~ 10 MeV. VOYAGER-1 provides a better constraint for lower DM masses depending on the choice of the galactic propagation models.

We show that the upcoming COSI, with a year of observation focusing towards the GC region, is going to provide a significant improvement to the above-mentioned constraints, thanks to its sensitivity towards the secondary photon emissions. For both the models, COSI can in principle probe a region of the parameter space that lies well beyond the reach of the existing indirect search or terrestrial experiments. For models like the kinetic-mixing case, where the CMB constraint is strong, COSI can probe values of $\langle\sigma v\rangle$ that are still well allowed by this constraint for a DM mass above ~ 100 MeV (based on mainly the ICS signal)

JCAP01(2026)038

as well as below $\sim 10\,\mathrm{MeV}$ (based on mainly bremsstrahlung, IfA and prompt photon signals) depending on the choice for the Galactic propagation.

To summarize, the present work highlights in detail the significance of leveraging the galactic DM annihilation induced secondary emissions to evaluate the indirect detection bounds on realistic sub-GeV DM models as well as the corresponding sensitivity projections from upcoming MeV telescopes like COSI.

Acknowledgments

We thank Peter Reimitz for useful discussions and collaboration in the initial stages of this work. We thank Pierre Salati for providing us with the VOYAGER-1 data. We also thank Lukas Simon and Andrea Caputo for useful discussions. M.C and A.K. acknowledge the hospitality of the Institut d'Astrophysique de Paris (IAP) where part of this work was done. M.C. also acknowledges the hospitality of the Flatiron Institute (Simons Foundation) and of the Physics Department of New York University.

Funding and research infrastructure acknowledgments: Research grant *DaCoSMiG* from the 4EU+ Alliance (including Sorbonne Université). Support from the Institut Henri Poincaré (UAR 839 CNRS-Sorbonne Université), and the LabEx *CARMIN* (ANR-10-LABX-59-01).

A Power emitted in different secondary processes

Here we describe the powers emitted in photons through different secondary processes considered in this work for the DM annihilation in the Galaxy.

- **Inverse Compton Scatterings (ICS):** the differential power emitted due to the IC scatterings of an $e^{\pm}$ on each ambient photon bath i in the interstellar radiation fields (ISRFs) is expressed as (see [43, 56, 90]),

$$\mathcal{P}^{i}_{\rm ICS}(E_\gamma, E_e, \vec{x}) = c\, E_\gamma \int d\epsilon\, n_i^{\rm ISRF}(\epsilon, \vec{x})\; \sigma_{\rm IC}(\epsilon, E_\gamma, E_e)\,, \tag{A.1}$$

  where $i \to$ CMB, infrared (IR) or starlight (SL) photon field, with the differential photon number density $n_i^{\rm ISRF}(\epsilon, \vec{x})$ (which is the same one used in [20, 21, 55, 57]). The quantity $\sigma_{\rm IC}$ denotes the Klein-Nishina cross-section, obtained from [43, 56, 90]. The limit of integration over the ambient photon energy ϵ in eq. (A.1) is determined by the kinematics of the IC scattering $1 \leq q \leq m_e^2/4E_e^2$, where $q \equiv \frac{E_\gamma m_e^2}{4\epsilon E_e(E_e - E_\gamma)}$. A graphical illustration of $P^i_{\rm ICS}$ (corresponding to the three ISRF components) as a function of the produced photon energy E_γ (for different input $e^{\pm}$ energies) can be found in [20]. The total power in the ICS process is obtained as: $\mathcal{P}_{\rm ICS} = \sum_{i \in \rm ISRF} \mathcal{P}^i_{\rm ICS}$.

- **Bremsstrahlung:** the bremsstrahlung power emitted due to the scattering of an $e^{\pm}$ (with $E_e > E_\gamma$) with the gas particles is given by (see [57]):

$$\mathcal{P}_{\rm brem}(E_\gamma, E_e, \vec{x}) = c\, E_\gamma \sum_i n_i(\vec{x})\, \frac{d\sigma_i^{\rm brem}}{dE_\gamma}(E_e, E_\gamma)\,. \tag{A.2}$$

  Here $n_i(\vec{x})$ describes the number density distribution of each of the gas species (ionic, atomic and molecular) and $\frac{d\sigma_i^{\rm brem}}{dE_\gamma}(E_e, E_\gamma)$ is the corresponding differential scattering

JCAP01(2026)038

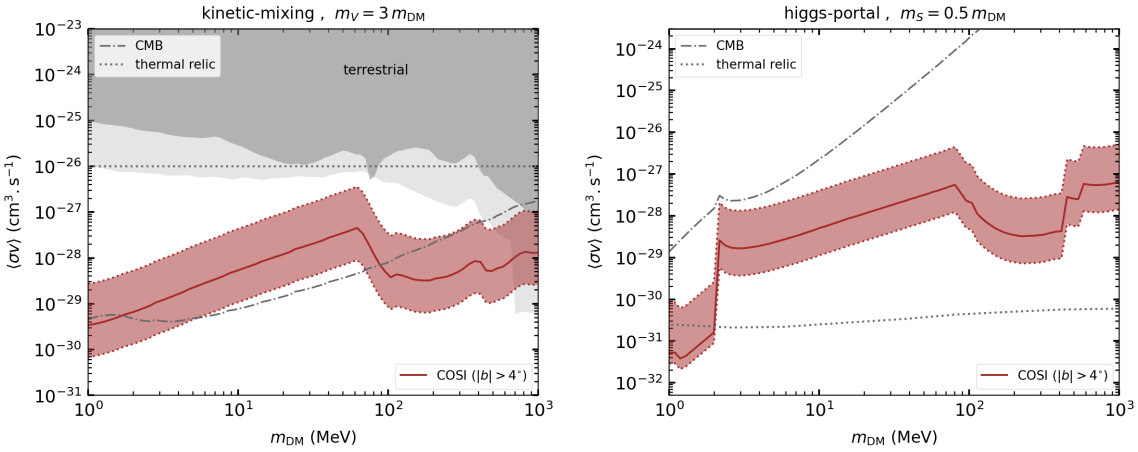

Figure 8. Effect of *varying the DM profile*. Brown solid line: the COSI projection obtained considering the NFW DM profile of eq. (3.1) (the same as the one shown in figure 6). Upper edge of the band: corresponding to the same Isothermal (cored) DM profile discussed in [55]. Lower edge of the band: corresponding to the Einasto profile from [54] (for the baryonic model B2) with the profile parameters adjusted within their 1σ uncertainty to maximize the J-factor (like in [24]).

cross-section for bremsstrahlung. The gas maps used here are the same ones used in [20, 21, 55, 57].

- **In-flight annihilation (IfA):** the power emitted due to the in-flight annihilation of an e^+ can be expressed as [16]:

$$\mathcal{P}_{\rm IfA}(E_\gamma, E_e, \vec{x}) = c\, E_\gamma\, n_{e^-}(\vec{x})\, \beta_e\, \frac{d\sigma^{\rm IfA}}{dE_\gamma}(E_e, E_\gamma)\,. \tag{A.3}$$

Here $\frac{d\sigma^{\rm IfA}}{dE_\gamma}(E_e, E_\gamma)$ is the differential cross-section related to the IfA process (see [16]), β_e is the dimensionless velocity of the e^+ and $n_{e^-}(\vec{x})$ is the number density of target electrons in the galactic medium (obtained from [57]). The kinematics for the process is $\gamma_e(1-\beta_e) \leq 2E_\gamma/m_e - 1 \leq \gamma_e(1+\beta_e)$, with $\gamma_e = E_e/m_e$.

B Dependence on the DM profile

In figure 8 we illustrate the effect of considering different DM profiles on the projected sensitivities of COSI, for the two considered DM models. In each case, the brown solid line corresponds to the projection obtained with the NFW profile of eq. (3.1) and is same as the one shown in figure 6. The associated brown band indicates the variation due to different choices for the DM profile. The upper edge of the band corresponds to the truncated Isothermal (cored) profile $\rho^{\rm Iso}_{\rm DM}(r) = \rho_0 / \left(1 + \left(\frac{r}{r_s}\right)^2\right)$, with the corresponding parameters $\rho_0 = 2.112\,{\rm GeV\,cm^{-3}}$ and $r_s = 4\,{\rm kpc}$ tabulated in [43] (also used in [55]). On the other hand, the lower edge of the band corresponds to the Einasto profile $\rho^{\rm Ein}_{\rm DM}(r) = \rho_0 \exp\left\{-\frac{2}{\alpha}\left(\left(\frac{r}{r_s}\right)^\alpha - 1\right)\right\}$ from [54] (corresponding the baryonic model B2) with the profile parameters adjusted within their 1σ uncertainty to maximize the J-factor (like in [24]). This corresponds to $\alpha \simeq 0.1$, $r_s \simeq 6.5\,{\rm kpc}$

JCAP01(2026)038

and $\rho_{\rm DM}(r_\odot) \simeq 0.4\,{\rm GeV\,cm^{-3}}$. Figure 8 shows that, depending on the choice of DM profile, the indirect detection constraints on the DM models presented in figure 6 can vary by a factor of a few in both directions.

References

[1] S. Knapen, T. Lin and K.M. Zurek, *Light Dark Matter: Models and Constraints*, *Phys. Rev. D* **96** (2017) 115021 [arXiv:1709.07882] [INSPIRE].

[2] C. Boehm, T.A. Ensslin and J. Silk, *Can Annihilating dark matter be lighter than a few GeVs?*, *J. Phys. G* **30** (2004) 279 [astro-ph/0208458] [INSPIRE].

[3] C. Boehm and P. Fayet, *Scalar dark matter candidates*, *Nucl. Phys. B* **683** (2004) 219 [hep-ph/0305261] [INSPIRE].

[4] P. Fayet, *U-boson production in e+ e- annihilations, psi and Upsilon decays, and Light Dark Matter*, *Phys. Rev. D* **75** (2007) 115017 [hep-ph/0702176] [INSPIRE].

[5] C. Boehm et al., *MeV dark matter: Has it been detected?*, *Phys. Rev. Lett.* **92** (2004) 101301 [astro-ph/0309686] [INSPIRE].

[6] J.L. Feng and J. Kumar, *The WIMPless Miracle: Dark-Matter Particles without Weak-Scale Masses or Weak Interactions*, *Phys. Rev. Lett.* **101** (2008) 231301 [arXiv:0803.4196] [INSPIRE].

[7] Y. Hochberg, E. Kuflik, T. Volansky and J.G. Wacker, *Mechanism for Thermal Relic Dark Matter of Strongly Interacting Massive Particles*, *Phys. Rev. Lett.* **113** (2014) 171301 [arXiv:1402.5143] [INSPIRE].

[8] Y. Hochberg et al., *Model for Thermal Relic Dark Matter of Strongly Interacting Massive Particles*, *Phys. Rev. Lett.* **115** (2015) 021301 [arXiv:1411.3727] [INSPIRE].

[9] E. Bertuzzo, C.J. Caniu Barros and G. Grilli di Cortona, *MeV Dark Matter: Model Independent Bounds*, *JHEP* **09** (2017) 116 [arXiv:1707.00725] [INSPIRE].

[10] L. Darmé, S. Rao and L. Roszkowski, *Light dark Higgs boson in minimal sub-GeV dark matter scenarios*, *JHEP* **03** (2018) 084 [arXiv:1710.08430] [INSPIRE].

[11] R. Essig et al., *Constraining Light Dark Matter with Diffuse X-Ray and Gamma-Ray Observations*, *JHEP* **11** (2013) 193 [arXiv:1309.4091] [INSPIRE].

[12] K.K. Boddy and J. Kumar, *Indirect Detection of Dark Matter Using MeV-Range Gamma-Ray Telescopes*, *Phys. Rev. D* **92** (2015) 023533 [arXiv:1504.04024] [INSPIRE].

[13] A.X. Gonzalez-Morales, S. Profumo and J. Reynoso-Córdova, *Prospects for indirect MeV Dark Matter detection with Gamma Rays in light of Cosmic Microwave Background Constraints*, *Phys. Rev. D* **96** (2017) 063520 [arXiv:1705.00777] [INSPIRE].

[14] A. Caputo, M. Negro, M. Regis and M. Taoso, *Dark matter prospects with COSI: ALPs, PBHs and sub-GeV dark matter*, *JCAP* **02** (2023) 006 [arXiv:2210.09310] [INSPIRE].

[15] K.E. O'Donnell and T.R. Slatyer, *Constraints on dark matter with future MeV gamma-ray telescopes*, *Phys. Rev. D* **111** (2025) 083037 [arXiv:2411.00087] [INSPIRE].

[16] R. Bartels, D. Gaggero and C. Weniger, *Prospects for indirect dark matter searches with MeV photons*, *JCAP* **05** (2017) 001 [arXiv:1703.02546] [INSPIRE].

[17] M. Boudaud, J. Lavalle and P. Salati, *Novel cosmic-ray electron and positron constraints on MeV dark matter particles*, *Phys. Rev. Lett.* **119** (2017) 021103 [arXiv:1612.07698] [INSPIRE].

JCAP01(2026)038

[18] M. Boudaud, T. Lacroix, M. Stref and J. Lavalle, *Robust cosmic-ray constraints on p-wave annihilating MeV dark matter*, *Phys. Rev. D* **99** (2019) 061302 [arXiv:1810.01680] [INSPIRE].

[19] R. Laha, J.B. Muñoz and T.R. Slatyer, *INTEGRAL constraints on primordial black holes and particle dark matter*, *Phys. Rev. D* **101** (2020) 123514 [arXiv:2004.00627] [INSPIRE].

[20] M. Cirelli, N. Fornengo, B.J. Kavanagh and E. Pinetti, *Integral X-ray constraints on sub-GeV Dark Matter*, *Phys. Rev. D* **103** (2021) 063022 [arXiv:2007.11493] [INSPIRE].

[21] M. Cirelli et al., *Putting all the X in one basket: Updated X-ray constraints on sub-GeV Dark Matter*, *JCAP* **07** (2023) 026 [*Erratum ibid.* **08** (2025) E02] [arXiv:2303.08854] [INSPIRE].

[22] S. Balaji, D. Cleaver, P. De la Torre Luque and M. Michailidis, *Dark matter in X-rays: revised XMM-Newton limits and new constraints from eROSITA*, *JCAP* **11** (2025) 053 [arXiv:2506.02310] [INSPIRE].

[23] P. De la Torre Luque, S. Balaji and J. Koechler, *Importance of Cosmic-Ray Propagation on Sub-GeV Dark Matter Constraints*, *Astrophys. J.* **968** (2024) 46 [arXiv:2311.04979] [INSPIRE].

[24] A. Coogan, L. Morrison and S. Profumo, *Precision gamma-ray constraints for sub-GeV dark matter models*, *JCAP* **08** (2021) 044 [arXiv:2104.06168] [INSPIRE].

[25] A. Coogan et al., *Hunting for dark matter and new physics with GECCO*, *Phys. Rev. D* **107** (2023) 023022 [arXiv:2101.10370] [INSPIRE].

[26] N. Bernal, J.P. Neto, J. Silva-Malpartida and F.S. Queiroz, *Enabling thermal dark matter within the vanilla L_μ-L_τ model*, *Phys. Rev. D* **112** (2025) 075042 [arXiv:2507.02048] [INSPIRE].

[27] T.-P. Tang et al., *Prospects for probing sub-GeV leptophilic dark matter with the future VLAST*, *JCAP* **11** (2025) 013 [arXiv:2505.05359] [INSPIRE].

[28] Y. Watanabe et al., *Sub-GeV dark matter and MeV gamma-ray detection with COSI*, *JHEP* **09** (2025) 078 [arXiv:2504.11810] [INSPIRE].

[29] T.T.Q. Nguyen, I. John, T. Linden and T.M.P. Tait, *Strong Constraints on Dark Photon and Scalar Dark Matter Decay from INTEGRAL and AMS-02*, arXiv:2412.00180 [INSPIRE].

[30] T.T.Q. Nguyen et al., *INTEGRAL, eROSITA and Voyager Constraints on Light Bosonic Dark Matter: ALPs, Dark Photons, Scalars, $B-L$ and L_i-L_j Vectors*, arXiv:2507.13432 [INSPIRE].

[31] S. Balan et al., *Resonant or asymmetric: the status of sub-GeV dark matter*, *JCAP* **01** (2025) 053 [arXiv:2405.17548] [INSPIRE].

[32] A. Cheek, P. Figueroa, G. Herrera and I.M. Shoemaker, *Sub-GeV Dark Matter Under Pressure from Direct Detection*, arXiv:2507.15956 [INSPIRE].

[33] C.-T. Lu, X.-Y. Luo and Z.-Q. Xia, *Exploring semirelativistic p-wave dark matter annihilation in minimal Higgs portal near supermassive black hole*, *Phys. Rev. D* **111** (2025) 095015 [arXiv:2412.19292] [INSPIRE].

[34] T. Linden, T.T.Q. Nguyen and T.M.P. Tait, *X-ray constraints on dark photon tridents*, *Phys. Rev. D* **112** (2025) 023026 [arXiv:2406.19445] [INSPIRE].

[35] A.K. Saha, *Searching for dark matter with MeVCube*, *Phys. Rev. D* **111** (2025) 123041 [arXiv:2501.13162] [INSPIRE].

[36] P.J. Fitzpatrick, H. Liu, T.R. Slatyer and Y.-D. Tsai, *New pathways to the relic abundance of vector-portal dark matter*, *Phys. Rev. D* **106** (2022) 083517 [arXiv:2011.01240] [INSPIRE].

JCAP01(2026)038

[37] M. Abdughani et al., *Muonphilic dark matter explanation of gamma-ray galactic center excess: a comprehensive analysis*, *JHEP* **07** (2022) 127 [arXiv:2111.02946] [INSPIRE].

[38] G. Mohlabeng, A. Mondol and T.M.P. Tait, *Radiative corrections to light thermal pseudo-Dirac dark matter*, *Phys. Rev. D* **111** (2025) 056003 [arXiv:2405.08881] [INSPIRE].

[39] G. Krnjaic, *Probing Light Thermal Dark-Matter With a Higgs Portal Mediator*, *Phys. Rev. D* **94** (2016) 073009 [arXiv:1512.04119] [INSPIRE].

[40] G. Arcadi, A. Djouadi and M. Raidal, *Dark Matter through the Higgs portal*, *Phys. Rept.* **842** (2020) 1 [arXiv:1903.03616] [INSPIRE].

[41] J. Alexander et al., *Dark Sectors 2016 Workshop: Community Report*, arXiv:1608.08632 [INSPIRE].

[42] LDMX collaboration, *Light Dark Matter eXperiment (LDMX)*, arXiv:1808.05219 [INSPIRE].

[43] M. Cirelli, A. Strumia and J. Zupan, *Dark Matter*, arXiv:2406.01705 [INSPIRE].

[44] A. Coogan, L. Morrison and S. Profumo, *Hazma: A Python Toolkit for Studying Indirect Detection of Sub-GeV Dark Matter*, *JCAP* **01** (2020) 056 [arXiv:1907.11846] [INSPIRE].

[45] A. Coogan et al., *Hazma meets HERWIG4DM: precision gamma-ray, neutrino, and positron spectra for light dark matter*, *JCAP* **11** (2022) 033 [arXiv:2207.07634] [INSPIRE].

[46] T. Sjostrand, S. Mrenna and P.Z. Skands, *A Brief Introduction to PYTHIA 8.1*, *Comput. Phys. Commun.* **178** (2008) 852 [arXiv:0710.3820] [INSPIRE].

[47] M. Cirelli et al., *PPPC 4 DM ID: A Poor Particle Physicist Cookbook for Dark Matter Indirect Detection*, *JCAP* **03** (2011) 051 [*Erratum ibid.* **10** (2012) E01] [arXiv:1012.4515] [INSPIRE].

[48] T. Plehn, P. Reimitz and P. Richardson, *Hadronic Footprint of GeV-Mass Dark Matter*, *SciPost Phys.* **8** (2020) 092 [arXiv:1911.11147] [INSPIRE].

[49] P. Reimitz, *MeV astronomy with Herwig?*, *PoS* **TOOLS2020** (2021) 008 [arXiv:2102.00041] [INSPIRE].

[50] Belle-II collaboration, *The Belle II Physics Book*, *PTEP* **2019** (2019) 123C01 [*Erratum ibid.* **2020** (2020) 029201] [arXiv:1808.10567] [INSPIRE].

[51] G. Krnjaic et al., *A Snowmass Whitepaper: Dark Matter Production at Intensity-Frontier Experiments*, arXiv:2207.00597 [INSPIRE].

[52] C. Antel et al., *Feebly-interacting particles: FIPs 2022 Workshop Report*, *Eur. Phys. J. C* **83** (2023) 1122 [arXiv:2305.01715] [INSPIRE].

[53] J.F. Navarro, C.S. Frenk and S.D.M. White, *The Structure of cold dark matter halos*, *Astrophys. J.* **462** (1996) 563 [astro-ph/9508025] [INSPIRE].

[54] P.F. de Salas et al., *On the estimation of the Local Dark Matter Density using the rotation curve of the Milky Way*, *JCAP* **10** (2019) 037 [arXiv:1906.06133] [INSPIRE].

[55] M. Cirelli and A. Kar, *Prospects of future MeV telescopes in probingweak-scale dark matter*, *SciPost Phys.* **19** (2025) 080 [arXiv:2503.04907] [INSPIRE].

[56] M. Cirelli and P. Panci, *Inverse Compton constraints on the Dark Matter e^+e^- excesses*, *Nucl. Phys. B* **821** (2009) 399 [arXiv:0904.3830] [INSPIRE].

[57] J. Buch, M. Cirelli, G. Giesen and M. Taoso, *PPPC 4 DM secondary: A Poor Particle Physicist Cookbook for secondary radiation from Dark Matter*, *JCAP* **09** (2015) 037 [arXiv:1505.01049] [INSPIRE].

JCAP01(2026)038

[58] C. Evoli et al., *Cosmic-ray propagation with DRAGON2: I. numerical solver and astrophysical ingredients*, *JCAP* **02** (2017) 015 [arXiv:1607.07886] [INSPIRE].

[59] C. Evoli et al., *Cosmic-ray propagation with DRAGON2: II. Nuclear interactions with the interstellar gas*, *JCAP* **07** (2018) 006 [arXiv:1711.09616] [INSPIRE].

[60] E. Orlando, *Imprints of Cosmic Rays in Multifrequency Observations of the Interstellar Emission*, *Mon. Not. Roy. Astron. Soc.* **475** (2018) 2724 [arXiv:1712.07127] [INSPIRE].

[61] M. Negro et al., *Unveiling the Origin of the Fermi Bubbles with MeV Photon Telescopes*, *Astrophys. J.* **927** (2022) 225 [arXiv:2111.10362] [INSPIRE].

[62] E.C. Stone et al., *Voyager 1 Observes Low-Energy Galactic Cosmic Rays in a Region Depleted of Heliospheric Ions*, *Science* **341** (2013) 1236408 [INSPIRE].

[63] A.C. Cummings et al., *Galactic Cosmic Rays in the Local Interstellar Medium: Voyager 1 Observations and Model Results*, *Astrophys. J.* **831** (2016) 18 [INSPIRE].

[64] G. Wang, B.-Y. Su, L. Zu and L. Feng, *Exploring sub-GeV dark matter physics with cosmic ray and future telescopes*, *Eur. Phys. J. C* **85** (2025) 1348 [arXiv:2503.22148] [INSPIRE].

[65] L. Bouchet et al., *Diffuse emission measurement with INTEGRAL/SPI as indirect probe of cosmic-ray electrons and positrons*, *Astrophys. J.* **739** (2011) 29 [arXiv:1107.0200] [INSPIRE].

[66] S.C. Kappadath, *Measurement of the Cosmic Diffuse Gamma-Ray Spectrum from 800 keV to 30 MeV*, Ph.D. thesis, University of New Hampshire, Durham, U.K. (1998), https://wwwgro.unh.edu/users/ckappada/thesis_stuff/thesis.html.

[67] FERMI-LAT collaboration, *The Fermi Galactic Center GeV Excess and Implications for Dark Matter*, *Astrophys. J.* **840** (2017) 43 [arXiv:1704.03910] [INSPIRE].

[68] K. Engel et al., *The Future of Gamma-Ray Experiments in the MeV-EeV Range*, in the proceedings of the *Snowmass 2021*, Seattle, U.S.A. (2022) [arXiv:2203.07360] [INSPIRE].

[69] J.A. Tomsick et al., *The Compton Spectrometer and Imager*, arXiv:1908.04334 [INSPIRE].

[70] J. Beechert et al., *Calibrations of the Compton Spectrometer and Imager*, *Nucl. Instrum. Meth. A* **1031** (2022) 166510 [arXiv:2203.00695] [INSPIRE].

[71] AMEGO collaboration, *All-sky Medium Energy Gamma-ray Observatory: Exploring the Extreme Multimessenger Universe*, arXiv:1907.07558 [INSPIRE].

[72] AMEGO TEAM collaboration, *AMEGO: Exploring the Extreme Multimessenger Universe*, *Proc. SPIE Int. Soc. Opt. Eng.* **11444** (2020) 1144431 [arXiv:2101.03105] [INSPIRE].

[73] E-ASTROGAM collaboration, *The e-ASTROGAM mission*, *Exper. Astron.* **44** (2017) 25 [arXiv:1611.02232] [INSPIRE].

[74] E-ASTROGAM collaboration, *Science with e-ASTROGAM: A space mission for MeV-GeV gamma-ray astrophysics*, *JHEAp* **19** (2018) 1 [arXiv:1711.01265] [INSPIRE].

[75] E. Orlando et al., *Exploring the MeV sky with a combined coded mask and Compton telescope: the Galactic Explorer with a Coded aperture mask Compton telescope (GECCO)*, *JCAP* **07** (2022) 036 [arXiv:2112.07190] [INSPIRE].

[76] GRAMS collaboration, *Overview of the GRAMS (Gamma-Ray AntiMatter Survey) Project*, *PoS* **ICRC2021** (2021) 653 [INSPIRE].

[77] S.D. Hunter et al., *A Pair Production Telescope for Medium-Energy Gamma-Ray Polarimetry*, *Astropart. Phys.* **59** (2014) 18 [arXiv:1311.2059] [INSPIRE].

JCAP01(2026)038

[78] X. Wu et al., *PANGU: A High Resolution Gamma-ray Space Telescope*, *Proc. SPIE* **9144** (2014) 91440F [arXiv:1407.0710] [INSPIRE].

[79] PLANCK collaboration, *Planck 2018 results. VI. Cosmological parameters*, *Astron. Astrophys.* **641** (2020) A6 [*Erratum ibid.* **652** (2021) C4] [arXiv:1807.06209] [INSPIRE].

[80] G. Steigman, B. Dasgupta and J.F. Beacom, *Precise Relic WIMP Abundance and its Impact on Searches for Dark Matter Annihilation*, *Phys. Rev. D* **86** (2012) 023506 [arXiv:1204.3622] [INSPIRE].

[81] H. Davoudiasl, D. Hooper and S.D. McDermott, *Inflatable Dark Matter*, *Phys. Rev. Lett.* **116** (2016) 031303 [arXiv:1507.08660] [INSPIRE].

[82] J.A. Evans et al., *Light Dark Matter from Entropy Dilution*, *JHEP* **02** (2020) 151 [arXiv:1910.06319] [INSPIRE].

[83] P. Asadi, T.R. Slatyer and J. Smirnov, *WIMPs without weakness: Generalized mass window with entropy injection*, *Phys. Rev. D* **106** (2022) 015012 [arXiv:2111.11444] [INSPIRE].

[84] F. D'Eramo, N. Fernandez and S. Profumo, *When the Universe Expands Too Fast: Relentless Dark Matter*, *JCAP* **05** (2017) 012 [arXiv:1703.04793] [INSPIRE].

[85] P.F. Depta, M. Hufnagel, K. Schmidt-Hoberg and S. Wild, *BBN constraints on the annihilation of MeV-scale dark matter*, *JCAP* **04** (2019) 029 [arXiv:1901.06944] [INSPIRE].

[86] N. Sabti et al., *Refined Bounds on MeV-scale Thermal Dark Sectors from BBN and the CMB*, *JCAP* **01** (2020) 004 [arXiv:1910.01649] [INSPIRE].

[87] T.R. Slatyer, *Indirect dark matter signatures in the cosmic dark ages. I. Generalizing the bound on s-wave dark matter annihilation from Planck results*, *Phys. Rev. D* **93** (2016) 023527 [arXiv:1506.03811] [INSPIRE].

[88] F. D'Eramo and S. Profumo, *Sub-GeV Dark Matter Shining at Future MeV γ-Ray Telescopes*, *Phys. Rev. Lett.* **121** (2018) 071101 [arXiv:1806.04745] [INSPIRE].

[89] J.H. Chang, R. Essig and S.D. McDermott, *Supernova 1987A Constraints on Sub-GeV Dark Sectors, Millicharged Particles, the QCD Axion, and an Axion-like Particle*, *JHEP* **09** (2018) 051 [arXiv:1803.00993] [INSPIRE].

[90] S. Colafrancesco, S. Profumo and P. Ullio, *Multi-frequency analysis of neutralino dark matter annihilations in the Coma cluster*, *Astron. Astrophys.* **455** (2006) 21 [astro-ph/0507575] [INSPIRE].

JCAP01(2026)038